Journal of Materials Chemistry A

ROYAL SOCIETY OF CHEMISTRY

PAPER

View Article Online
View Journal

Cite this: DOI: 10.1039/d6ta01360k

A fresh perspective on accelerated degradation studies for proton exchange membranes

R. Rameker, †[ab] J.-P. Poc, †[ac] S. Jovanovic, *[a] J. Park, [a] C. Oeß, [ac] J. Liu, [ac] S. Speer, [ac] L. Rein, [ac] K. Froehlich, [a] D. T. Daniel, [a] A. Windmüller, [a] H. Kungl, [a] S. Basak, [a] E. Jodat, [a] A. Karl, [a] J. Granwehr [ab] and Rüdiger-A. Eichel [acd]

Driven by the increasing demand for green hydrogen, proton exchange membrane (PEM) water electrolyzers are positioned as a key technology in the sustainable energy market. A primary concern for electrolysis cells remains the aspect of PEM durability. For durability testing, researchers often resort to accelerated degradation procedures utilizing *ex situ* Fenton reactions, exposing the PEM to high concentrations of Fe^{2+} and H_2O_2 to emulate prolonged exposure that mimics electrolysis conditions. However, these investigations often yield discrepancies compared to degradation occurring under actual long-term operation. The presented work elucidates and contextualizes *ex situ* Fenton testing by studying the transformations and reactions occurring across different length scales in state-of-the-art long- and short-side-chain PEM materials, revealing that the different weighting of chemical and morphological reaction pathways yields distinct degradation results for the two studied ionomers. PEM degradation mechanisms were classified into two pathways: chemical reactions, consisting of uniform polymer chain unzipping without significant preferential scissoring of polar moieties; and morphological transformations from the formation of voids, driven by pressure build-up inside the gas-impermeable membranes due to the breakdown of peroxide into oxygen. Both pathways operate in conjunction to affect crystallinity and ion conductivity, revealing that accelerated Fenton procedures require modification for transferable durability testing.

Received 12th February 2026
Accepted 16th April 2026

DOI: 10.1039/d6ta01360k

rsc.li/materials-a

Introduction

Green hydrogen is emerging as a crucial climate-neutral resource for industry, transportation, and the energy sector in global efforts to reduce CO_2 emissions.[1,2] However, the limited availability of high-purity green hydrogen remains a major challenge, especially given its demand in chemical, steel, petroleum, and fertilizer industries.[3] Proton exchange membrane (PEM) water electrolysis offers a promising route by converting renewable energy into high-purity hydrogen. Despite its advantages, widespread deployment of PEM water electrolyzers (PEMWEs) is hindered by their limited operational lifetime.[4,5] In particular, the membrane is highly vulnerable to mechanical, thermal, and chemical degradation, which compromises long-term reliability.[6–10] The benchmark membrane materials utilized for PEM water electrolysis are long- and short-side-chain (lsc- and ssc-) perfluorosulfonic acid (PFSA) ionomers.[11] Incorporation of transition metal ions into these ionomer membranes during electrolyzer operation has been reported in long-term studies.[12,13] In operating electrolyzers, cationic impurities such as Fe^{2+} can enter the membrane *via* two pathways: (i) exogenous contamination from the feed water, where even ASTM (American Society for Testing and Materials) Type II–compliant water contains residual ions, and (ii) endogenous contamination from stack component degradation or leaching during manufacturing and maintenance. Over time, such impurities can block a significant fraction of $-SO_3H$ groups in the membrane.[14,15] While this direct degradation pathway of ionomers may impact proton conductivity, it is fully reversible.

However, PEM literature concurs that transition metal cations strongly impact chemical degradation indirectly by catalyzing irreversible PEM decomposition mechanisms.[13,16] Of these mechanisms, the Fenton reaction is considered as a major pathway, where the breakdown of H_2O_2 to highly reactive radicals is catalyzed on transition metal ions with flexible oxidation state such as Fe^{2+} or Ti^{3+}.[17–19] In PEMWEs, H_2O_2 is present in low concentrations by *in situ* formation. During operation, O_2 is

[a]Institute of Energy Technologies - Fundamental Electrochemistry (IET-1), Forschungszentrum Jülich GmbH, Wilhelm-Johnen-Straße, 52425 Jülich, Germany. E-mail: s.jovanovic@fz-juelich.de
[b]Institute of Technical and Macromolecular Chemistry, RWTH Aachen University, 52056 Aachen, Germany
[c]Institute of Physical Chemistry, RWTH Aachen University, 52062 Aachen, Germany
[d]Faculty of Mechanical Engineering, RWTH Aachen University, Aachen, Germany
† These authors contributed equally.

generated at the anode and may permeate through the PEM to the cathode side in small amounts, particularly at high current densities[20] and under large anodic–cathodic pressure differentials.[21,22] Permeated O_2 is then electrochemically reduced at the platinum cathode in presence of absorbed H_2 on the platinum catalyst *via* a two-electron pathway (eqn (1)):

$$2H^+ + O_2 + 2e^- \rightarrow H_2O_2 \quad (1)$$

A recent study by Rui *et al.* also suggests direct oxidation of water to H_2O_2 in the anode compartment at high voltages.[23] Another relevant source for volatile renewable energy sources may also be the formation of H_2O_2 during system shutdown processes.[24] In the Fenton mechanism, H_2O_2 reacts catalytically with Fe^{2+}/Fe^{3+}, $HO^{\bullet}$, $H^{\bullet}$, and $HOO^{\bullet}$ radicals through sequential redox steps (eqn (2)–(4)):[25–27]

$$Fe^{2+} + H_2O_2 \rightarrow Fe^{3+} + OH^- + HO^{\bullet} \quad (2)$$

$$HO^{\bullet} + H_2 \rightarrow H^{\bullet} + H_2O \quad (3)$$

$$Fe^{3+} + H_2O_2 \rightarrow HOO^{\bullet} + Fe^{2+} + H^+ \quad (4)$$

Among the radicals formed, $HO^{\bullet}$ was reported to contribute to major degradation pathways in PEM ionomers despite significantly lower concentration compared to $H^{\bullet}$ and $HOO^{\bullet}$. $HO^{\bullet}$ initiates backbone unzipping, cleaving of sulfonic acid groups, and breaking of ether linkages, thereby disrupting the hydrophilic network and reducing conductivity.[17,28–30] These pathways diminish structural integrity and ion-exchange capacity, ultimately accelerating PEM failure (Fig. 1c and d). A detailed overview of additional radical-driven mechanisms is available in the literature.[17,25,27]

Although radical-induced degradation pathways are central to membrane failure, they typically evolve over thousands of operating hours in PEMWEs. The high cost of electrolysis test rigs and the long test durations make systematic screening and direct observation under real conditions unfeasible, especially when multiple membrane variants are compared. Therefore, Fenton degradation is usually studied using accelerated *ex situ* tests. *Ex situ* Fenton tests are performed either by immersing membranes in Fe^{2+}/H_2O_2 solution (solution method, Fig. 1a),[19,25,31–34] or by exchanging $-SO_3H$ moiety protons of the membrane with Fe^{2+} prior to H_2O_2 exposure (ion-exchange method, Fig. 1b).[32,35] Consequently, *ex situ* conditions often differ substantially from those in operating PEMWEs. A study by Fiedler *et al.* suggests an upper limit of 1 ppm Fe^{2+} in operating PEMWE,[36] compared to 10 to 100 ppm in reported *ex situ* Fenton studies.[31,32,35,37–45] Simultaneously, Fenton procedures utilize 10–30% H_2O_2 solutions, where PEMWE or PEM fuel cells exhibit several orders of magnitude lower levels.[31,32,35,37–45] While the high concentrations of reactants in *ex situ* testing accelerates PEM degradation, it also represents a limitation of current state-of-the-art testing methodology, as the impact of the stark difference in radical availability has been insufficiently addressed. In combination with substantially higher educt concentrations, the contrasting and competing reactions of radical generation and attacks may not only result in altered reaction kinetics, but also qualitatively different degradation processes. Thus, degradation of the ionomer may proceed differently, *e.g.*, favoring backbone *vs.* side chain degradation. Furthermore, the studies of Gubler *et al.* highlight the rate dependencies of radical recombination reactions, that may result in significant production of O_2 inside the ionomer at high radical concentrations, which has been insufficiently explored yet.[46]

Nonetheless, various analytical techniques have been utilized for the investigation of Fenton induced degradation in PEMs under *ex situ* test conditions. Both solid state and solution NMR spectroscopy provides molecular-level insight, but reports are highly inconsistent. In one study, pronounced signal loss was detected for SCF_2 groups, followed by OCF_2 and CF_2 side-chain resonances, while main-chain signals remained largely unaffected, thus indicating preferential cleavage of ether-linked side chains rather than the PTFE backbone.[31] A subsequent quantitative investigation confirmed that the concentration of backbone CF_2 groups remained constant, whereas side-chain functionalities degraded in the order $SCF_2 \approx \alpha\text{-}OCF_2 > CF_3 > \beta\text{-}OCF_2$, supporting the higher radical resistance of the polymer backbone.[37] In contrast, a separate study revealed that both backbone and side-chain integrals remained stable for approximately 12 h but began to shift upon extended exposure, suggesting that under prolonged oxidative stress, degradation of main and side chains may proceed concurrently.[35]

ATR-FTIR spectroscopy offers surface-sensitive information by probing specific bond vibrations and capturing local chemical changes of the membrane that is complementary to bulk sensitive NMR studies.[38] In line with NMR observations, ATR-FTIR studies report divergent findings regarding the chemical stability of PFSA membranes under Fenton treatment. In one investigations, normalized PTFE backbone vibration intensities remained constant, while SO_3 and C–O–C side-chain signals decreased with treatment time, indicating preferential attack at sulfonic acid groups and ether linkages.[39] Another study similarly observed a greater reduction in SO_3-associated bands than in C–F stretching bands, suggesting side-chain decomposition and an increased C–F/S–O peak ratio.[40] In contrast, several studies found no detectable variation in the relative intensities of backbone and side-chain vibrations, concluding that the overall chemical structure of the ionomer surface remained largely unchanged under both ion-exchange and solution method conditions.[32,41,42]

Despite inconsistencies in spectroscopic observations, Fenton treatment induces pronounced morphological changes in PEMs across the micrometer to millimeter scale, distinct from the membrane thinning typically reported in laboratory-scale PEMWE studies subjected to radical attack.[47,48] Scanning electron microscopy (SEM) provides the necessary spatial resolution to capture these features within the relevant size range, offering direct visualization of morphological degradation that complements chemical analyses. SEM analyses reveal that both solution- and ion-exchange-treated membranes develop surface blisters that grow, coalesce, and eventually form pinholes, while cross-sectional imaging shows a progressive appearance of

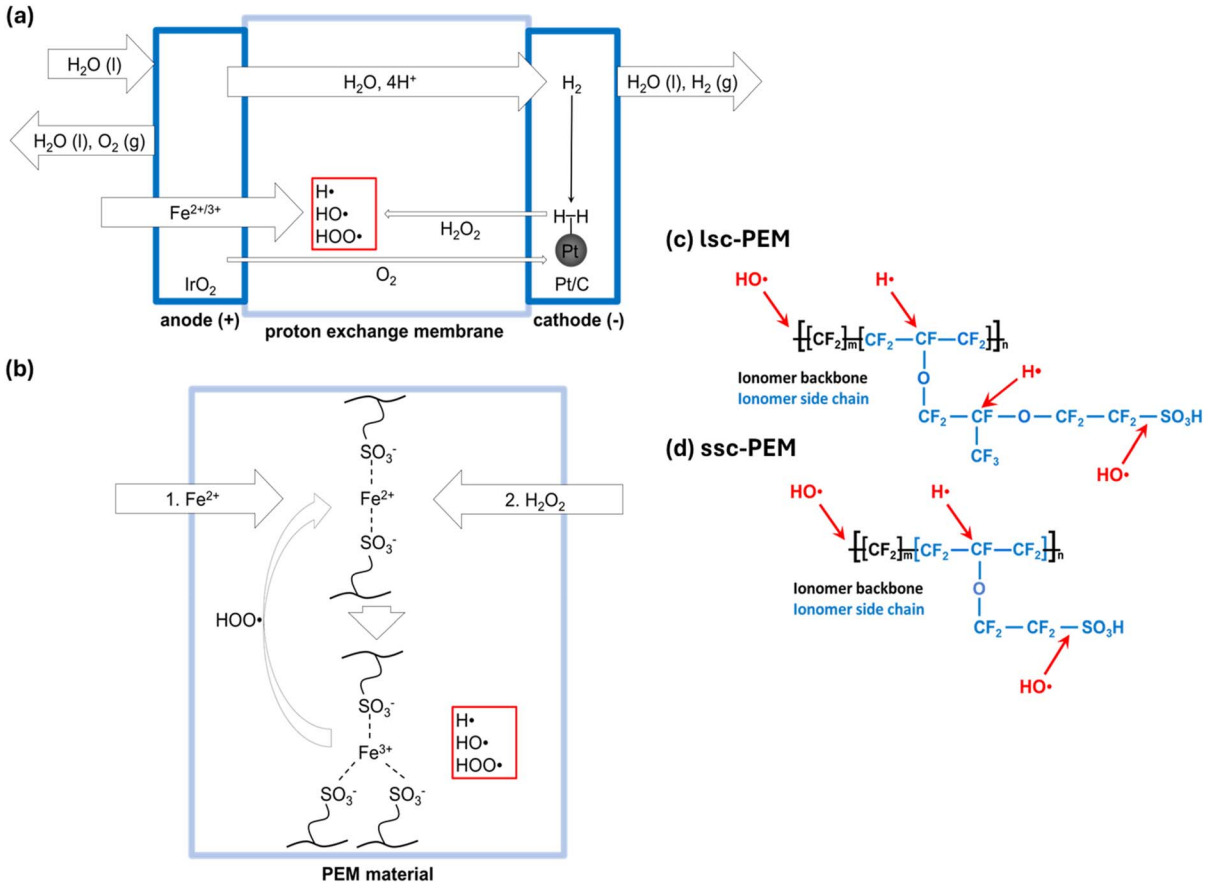

Fig. 1 Schematic illustration of radical generation pathways in (a) a proton-exchange membrane (PEM) water electrolyzer *via* the Fenton mechanism and (b) an *ex situ* Fenton test setup employing the ion-exchange method. Arrow widths represent relative transport and reaction rates. Panels (c) and (d) show the chemical structures of long side chain (lsc) and short side chain (ssc) PEMs with highlighted radical attack sites.

internal voids, which are absent in pristine membranes.[32,39,43–45] Minor variations, such as slightly larger blisters or increased foaming in one protocol, do not alter the central observation that Fenton treatment causes severe morphological deterioration.[32] Although the molecular effects of Fenton's reagent on PEMs remain debated, Fenton *ex situ* studies generally attribute the observed morphological changes to radical. A detailed overview of further characterization techniques and corresponding observations for *ex situ* Fenton treated PEMs is additionally provided in SI (Table S1).

The presented contrasting analytical studies highlight the absence of methodological standardization, thus complicating interpretation of *ex situ* Fenton studies. It is important to note that variations in test design (ion-exchange *vs.* solution methods), Fe^{2+}/H_2O_2 concentrations and solution replacement intervals may severely impact degradation behavior.[31,32,35,37–45] Post-treatment variability adds further uncertainty. Drying procedures can significantly affect results such as ATR-FTIR spectra, while incomplete iron removal may affect certain techniques, *e.g.* broadening of NMR signals and distortion side chain amplitudes in ATR-FTIR.[31,49,50] Such artifacts risk misrepresenting chemical degradation pathways, particularly the relative rates of side chain *versus* backbone cleavage.

These inconsistencies highlight the need for systematic, multimodal analysis of *ex situ* Fenton treated PEMs to clarify degradation pathways. To address this, the present study evaluates the effectiveness and limitations of *ex situ* Fenton tests for probing chemical degradation and provides a new perspective on how accelerated degradation protocols should be interpreted. Rather than proposing new mitigation strategies for PEM degradation, this study assesses the state-of-the-art assessment of chemical durability using complementary characterization techniques. Long- and short side chain PEMs were treated with Fenton's reagent by the ion-exchange method, which maximizes radical formation through Fe^{2+} incorporation. Following Fenton treatment, residual Fe^{2+}/Fe^{3+} was removed using a dedicated protocol, quantitative removal was confirmed by electron paramagnetic resonance (EPR) spectroscopy, while fluoride release was quantified by ion chromatography (IC). Chemical changes at the molecular scale were examined by ^{19}F NMR, ATR-FTIR, and Raman spectroscopy to identify preferential bond cleavage. Morphological changes at the nano-to mesoscale were probed by SEM, SAXS, and ^{19}F T_1 relaxation to monitor domain contraction, crystallinity, and chain mobility, complemented by contact angle and adhesion force measurements for surface properties. Finally, the macroscopic impact

on PEM performance was evaluated at the device level through current–voltage measurements to quantify ionic permeability.

Methods

Membrane preparation and Fenton treatment

Pristine long side chain PEMs (lsc-PEM; Nafion 115) were purchased from Fumatech BWT GmbH (Bietigheim-Bissingen, Germany), and short side chain PEMs (ssc-PEM; Aquivion E98-15S) from MSE Supplies, LLC (Tucson, Arizona, USA). PEMs were mounted in a home-built sample holder (Fig. S1) and placed in a 200 mL glass beaker. Heating was performed on heating and stirring plate in an oil bath. Prior to use, membranes were pretreated in 0.5 M H_2SO_4 at 80 °C for 5 h, followed by two neutralization steps in deionized (DI) water at 80 °C for 1 h each. After every step, samples were rinsed with DI water.

For the Fenton treatment, the PEMs were immersed in 0.5 M H_2SO_4 containing 1 M $FeSO_4$ at 80 °C for 5 h. Without removing the membrane from the holder, the assembly was rinsed with DI water and directly transferred into 30% v/v H_2O_2 solution in water preheated to 80 °C. The H_2O_2 solution was refreshed every 24 h, and samples remained immersed for the specified treatment duration.

Following Fenton treatment, PEMs were immersed in 0.5 M H_2SO_4 (100 mL) at 80 °C for 1 h, then treated in fresh 0.5 M H_2SO_4 containing disodium EDTA dihydrate (Na_2–EDTA; 7 mg per 50 mg PEM) for 1 h at 80 °C to remove residual iron.

Finally, PEMs were treated twice in fresh DI water at 80 °C for 1 h each.

Solid-state NMR spectroscopy (^{19}F MAS-NMR, T_1 relaxation) for molecular scale analysis

The ^{19}F magic angle spinning-nuclear magnetic resonance (MAS-NMR) spectra were recorded on a Bruker Avance III HD spectrometer using a Bruker Ascend 400WB (9.6 T, 400 MHz for ^{1}H) Magnet and a dual channel 1.3 mm MAS probe (PH MASDVT 400W1 BL1.3 N-P/H NO-I/E). The experiment temperature was maintained at 25 °C and the MAS spinning frequency was set to 40 kHz.

The ^{19}F center frequency was referenced to the $(CF_2)_n$ signal at −121 ppm, using a spectral width of 199.213 ppm. The recycle delay was set between 1 and 10 s, depending on the T_1 and 90° pulse lengths were set to 1.1–1.2 μs at 45 W.

Raw data were processed with a custom Python (Python v.3.9) script, applying 1 Hz exponential apodization and baseline correction using an Asymmetric Least Squares Smoothing algorithm.[51] The peak fitting was performed using LMFIT version 1.3.3 for Python 3.13 (64 bit), utilizing a non-linear least-squares algorithm.[52] Pseudo-Voigt functions were implemented to evaluate the integral, center frequency, full width at half maximum and the Pseudo-Voigt fraction of the signals. For the ssc-PEM, OCF_2, SCF_2 and CF_b signals were fitted using single Pseudo-Voigt functions. The $(CF_2)_n$ signal was fitted using three Pseudo-Voigt plus one Lorentzian profile[37] (center frequencies within the range from −121 to −123 ppm), which reduced the maximum residuals between data points and fit from >2% (with one Pseudo-Voigt profile used) to <1.5%, referenced to the amplitude of the $(CF_2)_n$ signal. For the lsc-PEM, the OCF_2 signal was fitted using two Pseudo-Voigt components while the CF_s signal at −144 ppm was fitted using a single Pseudo-Voigt profile.

The relative intensities of the SCF_2/CCF_2, OCF_2 and CF_b signals were normalized to the $(CF_2)_n$ integral *i.e.*, the sum of its fitted components. Errors were estimated by Gaussian error propagation with the root mean square of the noise per ppm determined from the range between −100 ppm and −90 ppm. Using

$$n_{\text{signal}} = 4\sigma n_{\text{ppm}} \tag{5}$$

, the noise of each signal was calculated with σ being the half-width at half maximum of a signal and n_{ppm} being the noise per ppm.

The ^{19}F T_1 relaxation time experiments were conducted utilizing the same experimental parameters as for the MAS experiments. The T_1 relaxation time constant was determined using a saturation recovery pulse sequence with 16 logarithmically spaced delays ranging from 0.008 to 7.5 s. The saturation train consisted of 256 equispaced pulses with 0.5 ms delay.

The data were analyzed by plotting the signal integrals as a function of delay time and fitting an exponential recovery function:

$$M_z = M_0 \cdot \left(1 - e^{-\frac{t}{T_1}}\right) \tag{6}$$

The T_1 error was derived from deviations of the exponential fit from the integral values.

Electron paramagnetic resonance (EPR) spectroscopy for iron detection

PEMs were cut into slices of approximately 15 × 2 mm and loaded into 4 mm EPR tubes under air. Continuous-wave EPR spectra were recorded on a Bruker ELEXSYS E580 spectrometer operating at 9.40 GHz. Measurements were performed at 20 K, with spectra acquired as first derivatives of the absorption function using a modulation amplitude of 0.15 mT, a modulation frequency of 100 kHz, and a microwave power of 4.743 mW.

ATR-FTIR spectroscopy for chemical bond analysis

Attenuated total reflectance Fourier-transform infrared (ATR-FTIR) spectra were recorded on a Spectrum 3 FT-IR/FIR spectrometer (PerkinElmer, UK) equipped with a Universal ATR accessory. 32 scans were averaged over 650 to 4000 cm^{-1} at 4 cm^{-1} resolution. For each PEM (pristine and Fenton treated), five different surface locations were measured to minimize inhomogeneity. Raw transmittance (%) data were converted to absorbance using:[53]

$$\text{Absorbance} = -\log_{10}\left(\frac{\text{Transmission}}{100}\right) \tag{7}$$

and baseline-corrected using an asymmetric least-squares algorithm $\lambda = 1 \times 10^5$, $p = 0.001$, 10 iterations).[51] Each spectrum was normalized to the PTFE backbone band at 1143 cm^{-1} ($\nu_s(CF_2)$).[54] For each sample, the five normalized spectra were averaged, and mean peak amplitudes were extracted and plotted *versus* Fenton treatment time. All data processing was performed using a custom Python script employing NumPy and pandas for numerical operations, and Matplotlib and Seaborn for plotting.[55–58]

Raman spectroscopy for backbone and sulfonic group analysis

PEMs were measured in a dry state; wet samples were air-dried overnight prior to measurement. Raman spectra were acquired on an Alpha 300R Raman microscope (WITec/Oxford Instruments, Ulm, Germany) equipped with a UHTS 300S spectrometer, a 300 g mm^{-1} grating, and a back-illuminated deep-depletion CCD camera. Measurements were performed using a Zeiss EC Epiplan-Neofluar Dic 20x/0.5 objective and a 785 nm laser (20 mW, 60 s acquisition).

For each sample, three spectra were recorded, background-corrected using the shape background subtraction tool in WITec Project 6.2, normalized to the CF_2 symmetric stretching vibration at 731 cm^{-1}, and averaged. In cases of strong fluorescence, time series of ten spectra were acquired to induce photobleaching; the final spectrum was then used for averaging.

Fluoride release quantified by ion chromatography (IC)

Fluoride release during Fenton treatment was quantified by IC. At each treatment time (0.25, 0.5, 1, 4, 8, 24 and 48 h), two 500 mL aliquots were taken from the liquid phase of the Fenton reagent for both membranes. Measurements were performed on a Metrohm IC 850 system (Metrohm AG, Herisau, Switzerland) using a Metrosep A SUPP 7-250 column with 3.6 mM Na_2SO_3 as eluent.

Fluoride concentration in solution (β_{F^-}, μg mL^{-1}) was determined, and the corresponding fluoride mass relative to membrane mass (w_{F^-}) was calculated as:

$$w_{F^-} = \beta_{F^-} \cdot \frac{V}{m_{eff}} \quad (8)$$

where V is the liquid phase volume and m_{eff} is the PEM mass in direct contact with the liquid phase. Errors were estimated by Gaussian error propagation, using $\Delta\beta_{F^-}$ (standard deviation of two-fold determination), ΔV (1% of liquid phase volume), and Δm_{eff} (5% of effective membrane mass). The higher error margins reflect evaporation losses and uncertainties in membrane hydration state.

Scanning electron microscopy (SEM) for morphology investigation

SEM imaging and cross-sectioning were performed on a Plasma FIB-SEM (AMBER X, TESCAN, Brno, Czech Republic). PEMs were mounted on aluminum stubs, dried at ambient conditions for 24 h, and degassed in the microscope chamber for 30 min. Surface micrographs were acquired at 2 keV accelerating voltage and 0.3 nA beam current using an Everhart–Thornley (E–T) secondary-electron detector. Cross-sections were prepared by trench milling with a 30 keV, 25 nA Xe^+ beam, followed by polishing at 30 keV, 5 nA, and imaged under the same 2 keV/0.3 nA conditions.

Quantitative blister-size analysis was carried out in ImageJ (v1.54p).[59] Individual blisters within a 3 mm field of view were manually segmented to measure diameters. Between 50 and 120 blisters per treated sample were analyzed to ensure representative statistics. The resulting diameters were processed using a Python script incorporating NumPy, Pandas and SciPy, and visualized as kernel density distributions using Matplotlib.[55–58,60]

Small angle X-ray scattering (SAXS) for nano structural analysis

SAXS experiments were performed on a XEUSS 3.0 UHR system (Xenocs, Sassenage, France) equipped with a Cu K_α source (λ = 1.5418 Å). Pristine and Fenton treated PEMs were clamped into 4 mm-diameter sample holders. Measurements were acquired at sample-to-detector distances of 42.5, 300, 1800, and 4500 mm with corresponding exposure times of 300, 300, 1800, and 1800 s. The measurements from the different sample-to-detector distances were merged to yield a total q-range of 0.0006–3.92 $Å^{-1}$ and evaluated regarding peak position and intensity using the proprietary software tool XSACT Pro (v. 2.10.3, Xenocs, Sassenage, France). Domain spacings (d) were calculated using the following relation for Bragg's distance:[61]

$$d = \frac{2\pi}{q} \quad (9)$$

Contact angle (θ) measurements for surface wettability

Sessile-drop contact angles of pristine and Fenton treated PEMs (stored in DI water prior to measurement) were recorded at room temperature on an OCA 200 goniometer (DataPhysics Instruments, Germany) using 4 μL water droplets. Contact angles were evaluated with SCA 20 software (DataPhysics Instruments) and measured immediately after the water droplet was placed on the sample surface. For each sample, five measurements were taken at different positions and averaged; results are reported as mean ± standard deviation (SD).

Adhesion force (F) measurements for interfacial properties

Adhesion forces (F) between the PEM and the analyte (4 μL of water droplets) were measured using a DCAT 25 tensiometer (DataPhysics Instruments GmbH, Germany) equipped with a CCD camera. PEMs were stored in DI water prior to use. The analyte was suspended on a ring holder (inner diameter 6.2 mm, outer diameter 6.6 mm) connected to a microbalance, and the balance was zeroed before measurement. The measurements for water adhesion were performed in air. The PEM approached the water droplet at 0.03 mm s^{-1}, compressing it by 0.3 mm. Three locations per sample were probed, and adhesion forces were calculated from the recorded force data.

Current–voltage (*I–V*) characterization

Current–voltage (*I–V*) measurements were performed to evaluate transmembrane ion transport. Pristine and Fenton treated PEMs (stored in DI water prior to use) were mounted in a custom-built two-compartment electrochemical cell with a circular opening of 0.28 cm^2 (sample area under investigation, Fig. S9). Each compartment was filled with 20 mL of 100 mM H_2SO_4 electrolyte, and the transmembrane potential was measured using Ag/AgCl reference wires (1 mm diameter) inserted into each compartment.[62,63]

Measurements were performed at ambient conditions (22 ° C) on a VSP-300 potentiostat (BioLogic, France). Ionic current flow throughout the PEM was monitored by applying a scanning triangle voltage from +100 mV to −100 mV in 10 mV steps. The last of 10 cycles was used for analysis. For visualization, a y-shift correction was performed.

Results

Molecular scale degradation probed by ^{19}F MAS-NMR

The ^{19}F MAS-NMR spectra of pristine, hydrated lsc-PEM (Fig. 2a) and ssc-PEM (Fig. 2b) are in line with their reported structures (Fig. 2e and f, respectively) and with literature studies.[37,64] Due to their identical PTFE backbone, the spectra only differ in their polar side chain contributions. For the ssc-PEM, the signal at −80 ppm is weaker and shifted to −79 ppm, reflecting the absence of a CF_3 group and the presence of only one OCF_2 moiety. Moreover, the component at −143 ppm is missing due to the lack of a branching point in the short side chain.

The ^{19}F MAS-NMR spectrum of the ssc-PEM significantly changes after 0.5 h of Fenton treatment (Fig. 2c). At this stage, no H_2SO_4 purification was conducted to remove catalytic iron. In the presence of the paramagnetic Fe^{2+} and Fe^{3+} ions, a strong broadening of the side chain signals OCF_2, SCF_2/CCF_2, and CF_b was observed. In particular, the OCF_2 and CF_b signals disappear almost completely. This is due to strong interactions between the nuclear spins and unpaired electron spins, leading to a significant reduction in T_2 relaxation time and thus to line-broadening.[65]

However, spectra can be restored after subsequent washing with H_2SO_4 to remove Fe^{2+}/Fe^{3+}-ions quantitatively. The post-treated ssc-PEM (Fig. 2d) showed comparable signal intensity and linewidth to the pristine ssc-PEM with only minor variations. This indicates that significant parts of the spectral changes between Fig. 2b and c reflect the paramagnetic influence of the foreign ions rather than changes in the chemical structure of ssc-PEM.

Removal of residual iron verified by EPR spectroscopy

Clear evidence of the effectiveness of this post-treatment method is provided by the EPR spectra of the post-treated and non-post-treated ssc-PEMs (Fig. 3a). While the EPR spectrum of the Fenton treated ssc-PEM exhibited evidence of paramagnetic Fe^{3+}-ions, whereas the Fenton and post-treated ssc-PEM did not. A corresponding EPR spectrum demonstrating the post-treatment effectiveness for the lsc-PEM is provided in the SI (Fig. S2).

The impact of Fenton treatment time on iron coordination is further explored in Fig. 3b. Both ionomers exhibited three major signals: $g = 1.99$ (Fe^{3+} dipole–dipole interactions),[66] $g_{eff} = 4.21$ (isolated Fe^{3+} in tetrahedral coordination),[66] and $g_{eff} = 8.56$ (high-spin Fe^{3+} in a strong field ligand site with low symmetry).[67] The lower intensity of the signal at $g = 1.99$ and the higher intensity of the signals at $g_{eff} = 4.21$ and $g_{eff} = 8.56$ indicate that Fe^{3+} ions in the lsc-PEM were more isolated. In comparison, the ssc-PEM exhibited more of a clustered Fe^{3+} environment after 24 h.[66] After 48 h, $g_{eff} = 4.21$ and $g_{eff} = 8.56$ intensities remained constant, while $g = 1.99$ intensities switched, suggesting an influence of the catalytic activity on the arrangement of the Fe^{3+}-ions in the ionomer structure.

Molecular scale insights from ^{19}F MAS-NMR signal ratios

Based on the deconvolution of the ^{19}F MAS-NMR spectra, the relative signal contributions of each molecular site were determined relative to the backbone signal intensity to study preferential degradation reactions of the lsc-PEM (Fig. 4a–d) and the ssc-PEM (Fig. 4e–g). While the SCF_2/CCF_2 signal of the lsc-PEM decayed by about 18% during Fenton treatment, the other signals remained constant over the entire period, considering the statistical error of each fit. This suggests preferential loss of sulfonic acid functionality. However, the other functional groups of the side chain do not appear to be degraded to the same extent.

In contrast to the lsc-PEM, for the ssc-PEM the relative signal intensity of no particular group was reduced within the margins of error. Thus, in the ssc-PEM the spectra suggest sequential rather than targeted side chain degradation. Therefore, ^{19}F MAS-NMR reveals a higher resistance against preferential side chain degradation for the bulk of ssc-PEM compared to the lsc-PEM.

Chemical degradation probed by ATR-FTIR and Raman spectroscopy

ATR-FTIR spectroscopy was used on pristine and Fenton treated PEMs to verify and support the NMR-based assessment of chemical degradation. For both pristine lsc- and ssc-PEMs, vibrational bands corresponding to COC (969 cm^{-1}; 982 cm^{-1}, lsc-PEM-specific) and SO_3^- (1056 cm^{-1}) were detected (Fig. 5a and c, respectively).[54]

For the lsc-PEM, normalized peak amplitudes remained near pristine values across all treatment times, showing only minor transient fluctuations (Fig. 5b). The ssc-PEM displayed similarly small variations for treatment times up to 1.5 h, but at 24, 48, and 72 h the mean amplitudes at 969 cm^{-1} and 1056 cm^{-1} were slightly lower than those of the pristine membrane, suggesting loss of the corresponding chemical groups after prolonged exposure (Fig. 5d). In both PEMs, values of treated samples were generally close to the standard deviation range of the pristine sample, indicating that any loss of C–O or S–O bonds under the applied Fenton treatment conditions was minimal. Raman spectroscopy provided complementary confirmation, with no significant changes detected in the relevant vibrational modes

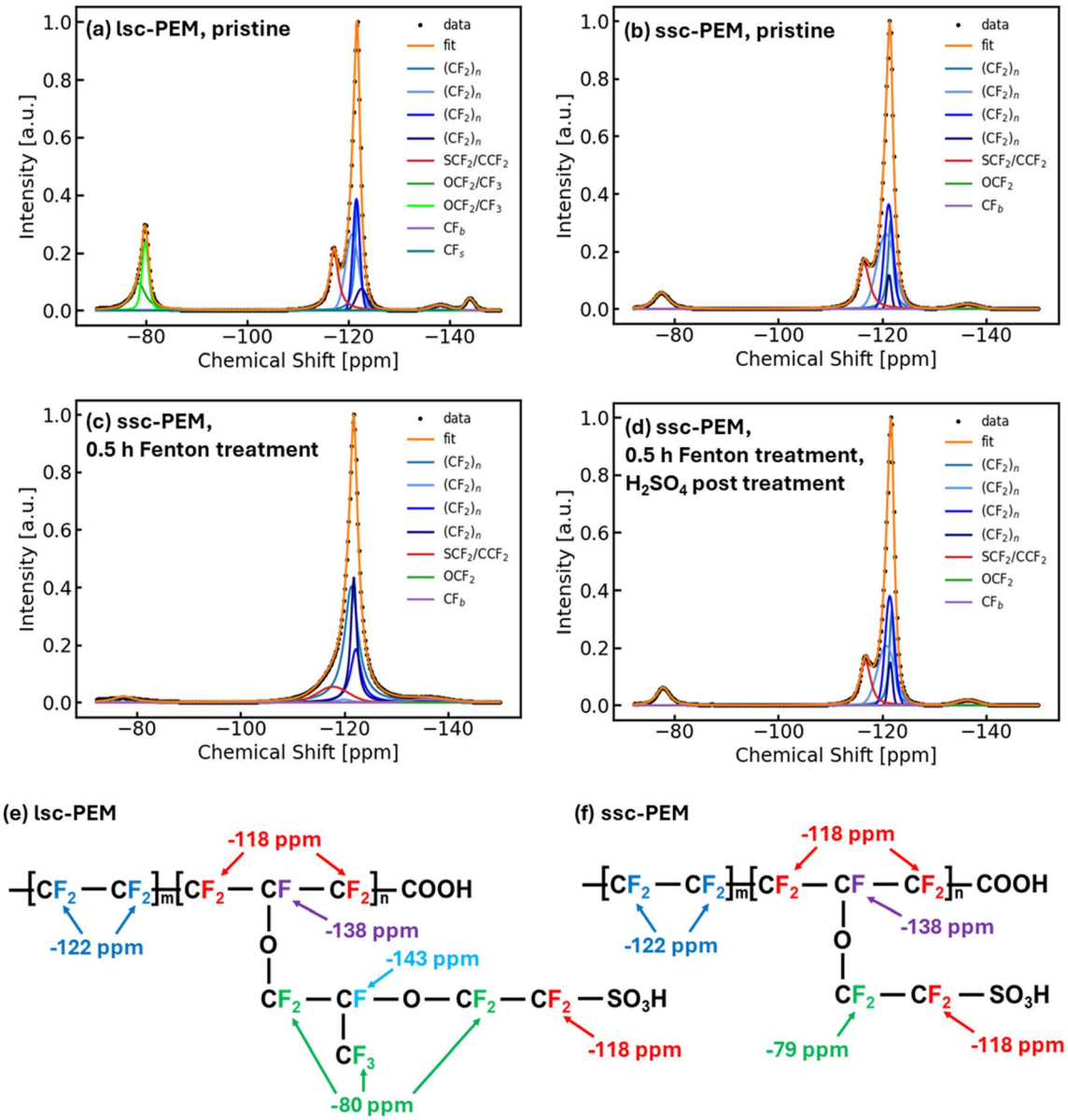

Fig. 2 ^{19}F MAS-NMR spectra of hydrated (a) lsc-PEM and (b) ssc-PEM in the pristine state, and of (c) ssc-PEM after 0.5 h of Fenton treatment and (d) after additional post-treatment with 0.5 M H_2SO_4. Spectra were recorded at a spinning frequency of 30 kHz. Experimental data are shown as black dots, the fit as an orange line, and individual Lorentzian and Pseudo-Voigt components in the colors indicated in the legend. Panels (e) and (f) show chemical structures with ^{19}F signal assignments for lsc-PEM and ssc-PEM, respectively.

after treatment (Fig. S3 and S4). The normalized, averaged ATR-FTIR spectra of pristine and treated PEMs are provided in the SI (Fig. S5 and S6).

Fluoride release as a marker of chemical breakdown revealed by IC

To classify the qualitative alterations of the PEM structure derived from ^{19}F MAS-NMR and ATR-FTIR quantitatively, the fluoride release rate of both ionomers as a function of Fenton treatment time (Fig. 6) was determined using IC. For both PEMs, the amount of fluoride in the liquid phase of the Fenton reagent increased rapidly within the first hour of treatment. During the next 23 h, the levels of released fluoride remained nearly constant. However, replacing the Fenton reagent with a fresh 30% H_2O_2 solution after 24 h increased the fluoride release by more than one order of magnitude for both PEMs. This may reflect transport limitations due to steric hindrance from ionomer fragments. By the addition of a fresh, highly concentrated hydrogen peroxide solution, these sterically demanding fragments may also have been broken down into smaller units, enabling the release of increased amounts of fluoride.

Assuming the membrane was completely dehydrated during weighing, the proportion of fluoride release in the total fluorine contained in the sample was calculated as 7.14% (48.138 μg mg_{sample}^{-1}) for the lsc-PEM and 19.26% (130.67 μg mg_{sample}^{-1})

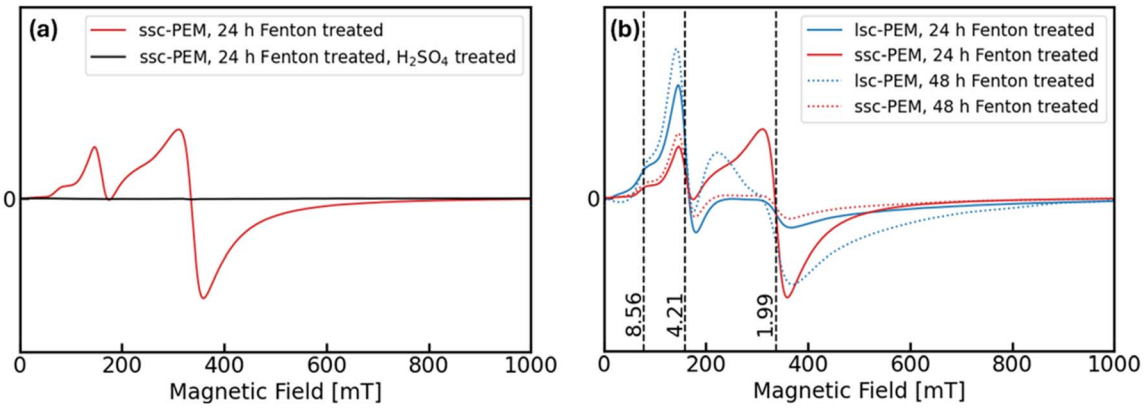

Fig. 3 Continuous-wave EPR spectra of (a) ssc-PEM after 24 h of Fenton treatment (red) and after additional post-treatment with 0.5 M H_2SO_4 (black), and (b) lsc-PEM (blue) and ssc-PEM (red) after 24 h (solid lines) and 48 h (dashed lines) of Fenton treatment. Vertical dashed lines at $g = 1.99$, $g_{eff} = 4.21$ and $g_{eff} = 8.56$ indicate reference positions.

for the ssc-PEM. At this proportion of released fluoride, the influence of Fenton degradation can certainly be regarded as significant. Notably, the ssc-PEM released nearly three times more fluoride than the lsc-PEM.

Overall, IC complements the information drawn qualitatively from the ^{19}F MAS-NMR spectra with a quantitative assessment of degradation. While spectroscopy collectively indicates that Fenton treatment induces only minor or negligible degradation on the molecular level, IC reveals significant fluoride release.

Morphological changes revealed by SEM

Upon Fenton treatment, both lsc-PEM and ssc-PEM changed from clear, transparent sheets to light yellow, opaque films. Although subsequent iron removal eliminated the yellow coloration, the membranes remained opaque, indicating irreversible bulk structural and morphological changes. Similar transparency loss has been reported in other *ex situ* Fenton studies.[39,43]

SEM analysis (Fig. 7) revealed progressive blister formation in both membrane types, with overall blister density increasing with treatment time, consistent with *ex situ* Fenton studies.[39,43]

In the lsc-PEM, blister nucleation occurred rapidly, followed by growth and coalescence. The size distribution shifted toward larger radii and broadened substantially at longer treatment times, reflecting the merging of adjacent blisters into irregular structures with poorly defined borders. This trend mirrors

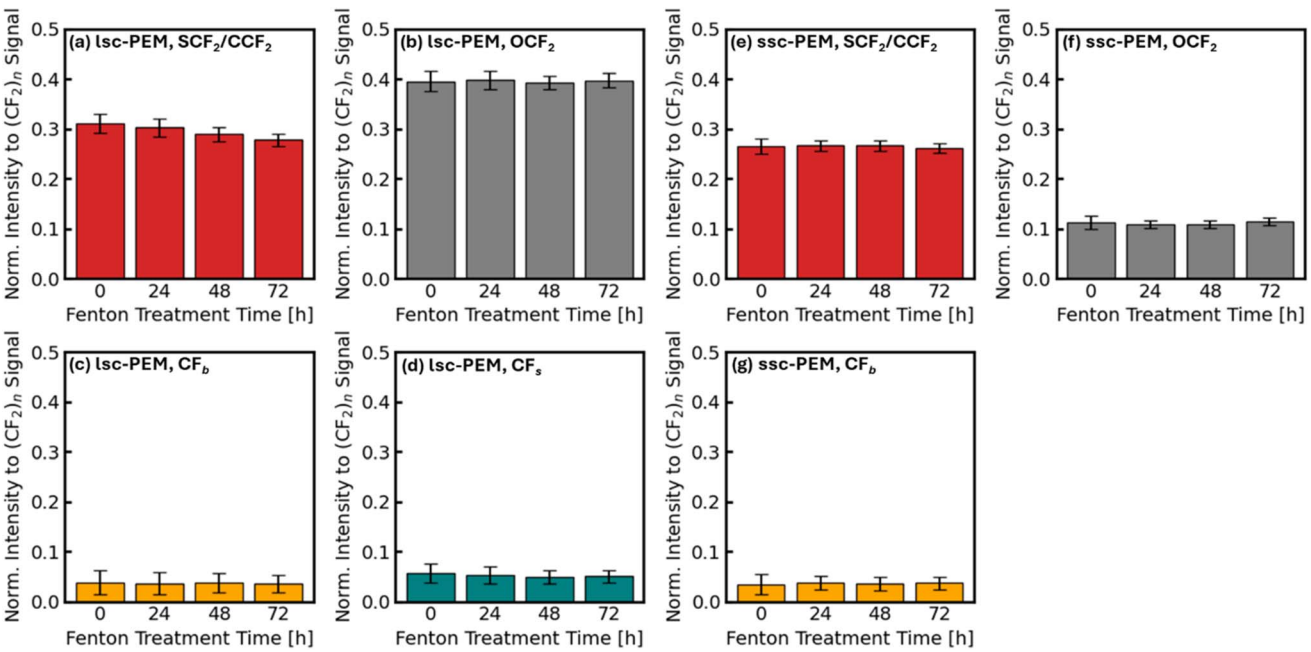

Fig. 4 Relative intensities of SCF_2/CCF_2 (red), OCF_2 (grey), CF_b (orange) and CF_s (teal) signals calculated from the ^{19}F spectra of (a–d) lsc-PEM and (e–g) ssc-PEM. Data are shown for pristine hydrated membranes and after 24 h, 48 h, and 72 h of Fenton treatment. Error bars were estimated by Gaussian error propagation as described in the methods.

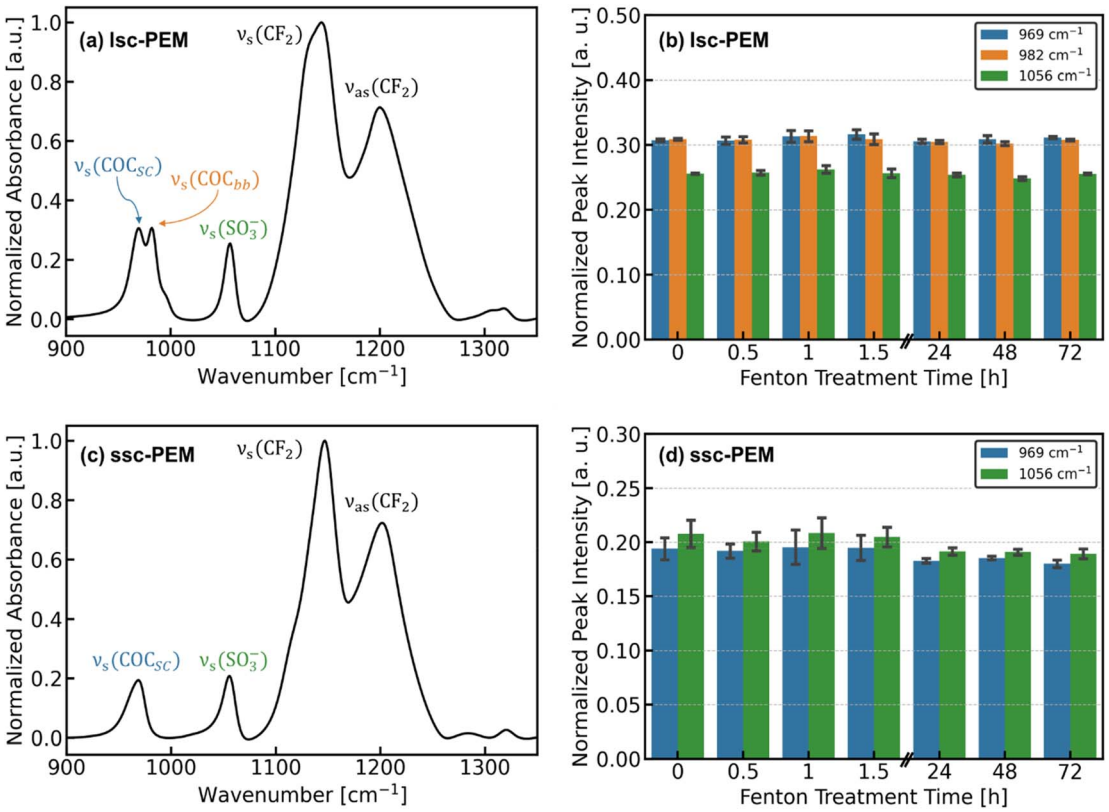

Fig. 5 ATR-FTIR analysis of (a and b) lsc-PEM and (c and d) ssc-PEM before and after Fenton treatment. Panels (a) and (c) show normalized absorbance spectra in the 900–1350 cm^{-1} region for pristine membranes, with highlighted vibrational bands (969 cm^{-1} ($\nu_s(COC_{bb})$), blue; 982 cm^{-1} ($\nu_s(COC_{bb})$), orange; lsc-PEM only); 1056 cm^{-1} ($\nu_s(SO_3^-)$), green). Panels (b) and (d) present the corresponding normalized peak amplitudes as a function of Fenton treatment time. Error bars represent standard deviations.

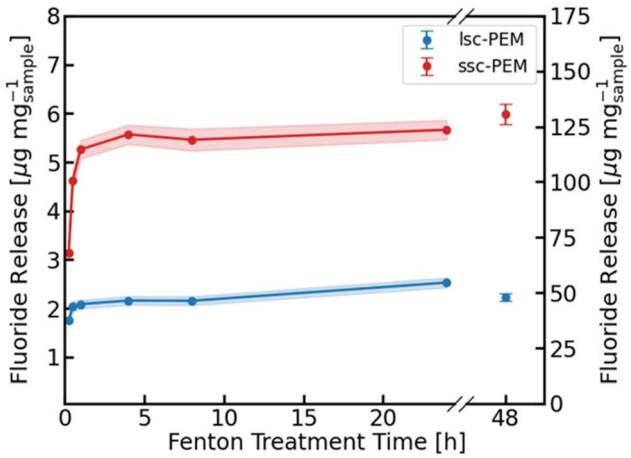

Fig. 6 Fluoride release rate *via* IC as a function of Fenton treatment time for lsc-PEM (blue) and ssc-PEM (red). Data are normalized to sample mass (μg mg^{-1}). Time points include 0.25, 0.5, 1, 4, 8, 24 h (left *y*-axis), and 48 h (right *y*-axis). Shaded areas represent error ranges estimated by Gaussian error propagation as described in the methods.

previous observations of defect enlargement during extended Fenton treatment.[39,44]

In contrast, ssc-PEM developed blisters more slowly, which remained uniformly smaller throughout exposure. The size distribution stayed narrow, with little shifting and no significant broadening, indicating limited coalescence. Individual blisters retained well-defined borders, and this stability was consistent across independently treated samples, suggesting greater resistance to blister merging under prolonged Fenton treatment.

Close inspection of surface protrusions in both membranes (Fig. S7) revealed four recurring morphologies: intact rounded blisters, burst-cap blisters, slit-like tears, and collapsed "volcano" structures, all previously documented.[39,43,44] Cross-sectional cuts through these features (Fig. S8) exposed underlying voids, in agreement with earlier *ex situ* Fenton studies.[32,39]

In summary, Fenton treatment induced pronounced blistering in both membranes. Lsc-PEM exhibited rapid blister growth, distribution broadening, and extensive coalescence, whereas ssc-PEM maintained smaller, discrete blisters with a consistently narrow distribution, likely reflecting differences in side chain length.

Crystallinity, nano- and mesoscale structure by SAXS

SAXS was used to examine changes in crystalline and hydrophilic domain (*d*)-spacings in pristine and Fenton treated membranes (Fig. 8a, lsc-PEM; Fig. 8b, ssc-PEM).

In the pristine state, the matrix knee, corresponding to intercrystalline *d*-spacings, appears at $q = 0.058$ Å^{-1} ($d = 108$ Å)

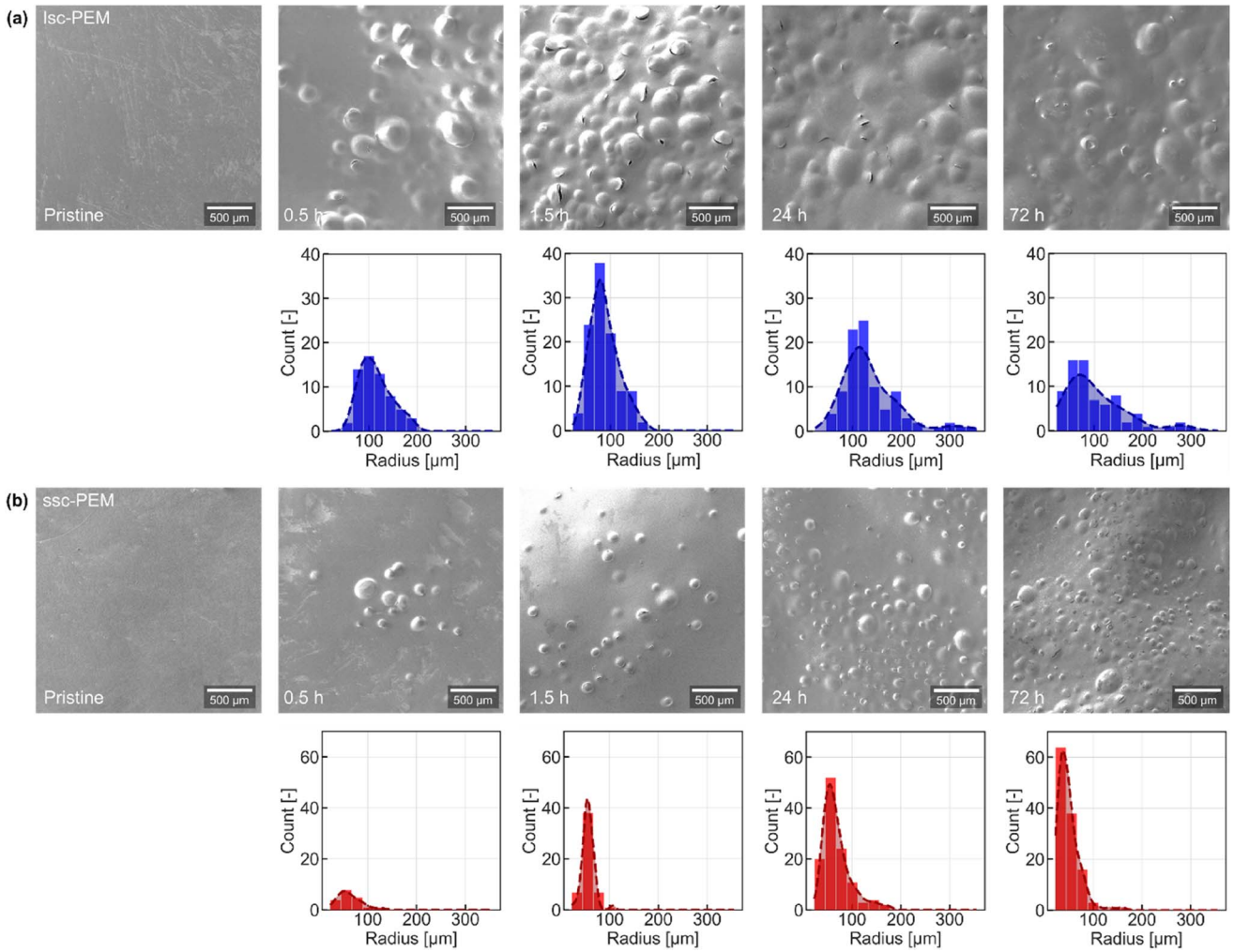

Fig. 7 SEM analysis of surface blistering in (a) lsc-PEM and (b) ssc-PEM before and after Fenton treatment. Micrographs show surface morphology at increasing exposure times. Blister size distributions are presented for both membranes, with lsc-PEM shown in blue and ssc-PEM in red.

for the lsc-PEM and $q = 0.056$ Å^{-1} ($d = 112$ Å) for the ssc-PEM.[61,68] The slightly smaller d-spacing of the lsc-PEM is consistent with its longer nonionic backbone, which promotes the growth of larger crystallites.[61] The ionomer peak, correlating to the hydrophilic d-spacings, occurs at $q = 0.22$ Å^{-1} ($d = 28.6$ Å) for lsc-PEM and $q = 0.27$ Å^{-1} ($d = 23.3$ Å) for ssc-PEM, with lower intensity in the latter, likely due to its shorter ionic side chains.[61,68] In the WAXS region, both membranes exhibit reflections at $q = 1.20$ Å^{-1} ($d = 5.2$ Å, intermolecular chain spacing, WAXS Peak 1) and $q = 2.75$ Å^{-1} ($d = 2.3$ Å, intramolecular distance, WAXS Peak 2), with comparable peak positions and intensities.[68,69]

Fenton treatment progressively attenuates the matrix knee in both membranes, indicating a loss or disordering of crystalline domains.[61] In the lsc-PEM, this feature partially recovers at 72 h, suggesting recrystallization. In the ssc-PEM, a slight upturn emerges at low q (~0.003 Å^{-1}), consistent with polymer aggregation.[69] The ionomer peak, correlating to the hydrophilic d-spacing, of the lsc-PEM shifts from $q = 0.22$ Å^{-1} ($d = 28.6$ Å) to $q = 0.24$ Å^{-1} ($d = 26.2$ Å), indicating shorter distances between the hydrophilic domains, while the ionomer peak of the ssc-PEM remains unchanged and becomes no longer visible after extended Fenton treatment. This observation supports the assumption of an increasing loss of mesoscale order in the membrane.

In the WAXS region both membrane types retain their original reflection positions and intensities, exemplifying that Fenton treatment does not alter the crystallinity of the polymer backbone itself.

Overall, Fenton treatment leads to a loss of mesoscale order in both the crystalline hydrophobic domains—evidenced by complete attenuation of the matrix knee—and the hydrophilic domains, as shown by a shift and reduction of the ionomer peak. It is observed that hydrophilic domain crystallinity decreases more strongly in the lsc-PEM than in the ssc-PEM. Feature assignments for pristine membranes are given in Table S2, and changes after Fenton treatment are summarized in Table S3.

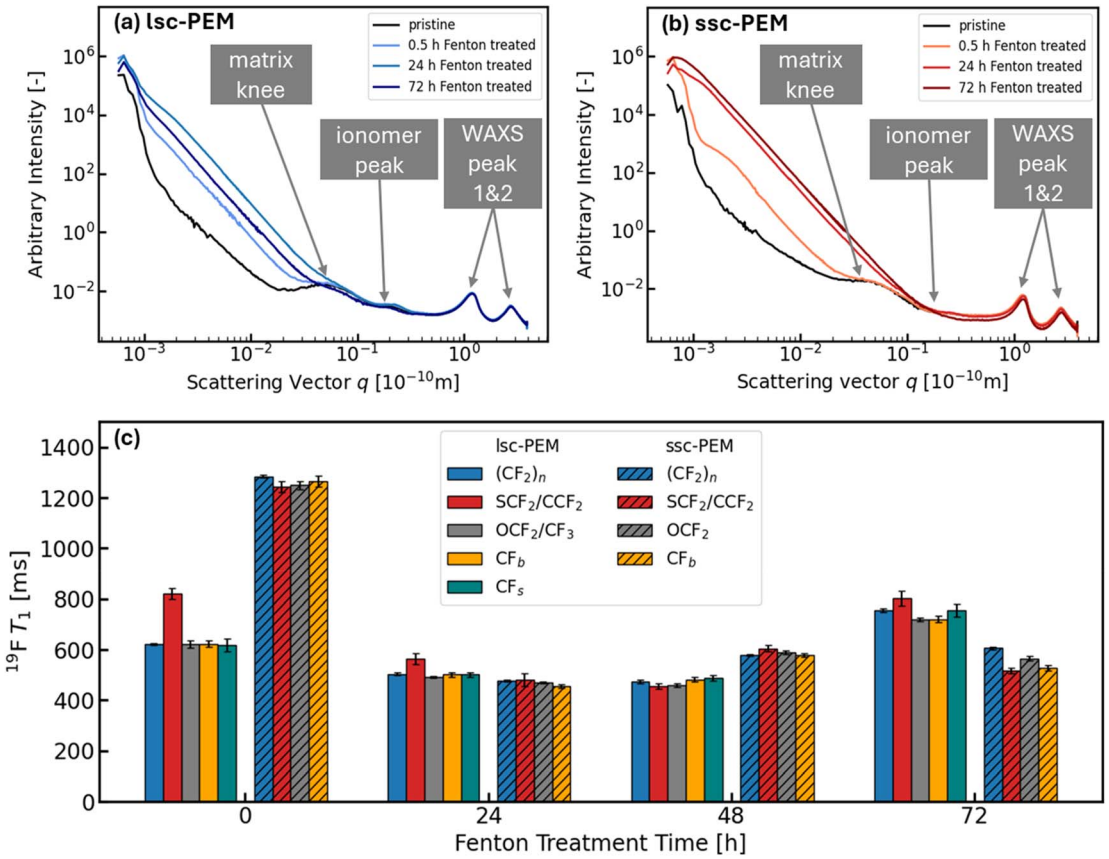

Fig. 8 | SAXS profiles of the lsc-PEM (a) and ssc-PEM (b) in the pristine state and after 0.5, 24, and 72 h of Fenton treatment. (c) ^{19}F T_1 relaxation times of selected fluorine environments in the lsc-PEM (solid bars) and ssc-PEM (hatched bars) for pristine membranes and after 24, 48, and 72 h of treatment. Shown are the $(CF_2)_n$ (blue), SCF_2/CCF_2 (red), OCF_2/CF_3 (grey), CF_b (orange), and CF_s (teal) environments. Error bars represent deviations of the exponential fit from the integral values. The T_1 error was calculated by regression analysis of the exponential fit of the integral values.

Polymer-chain mobility probed by ^{19}F T_1 relaxation

^{19}F spin-lattice relaxation (T_1) measurements were performed on pristine and Fenton treated membranes to correlate polymer-chain mobility and crystallinity changes inferred from SAXS. As shown in Fig. 8c, ^{19}F T_1 across all groups evolved with Fenton treatment time for both PEMs, reflecting the impact of Fenton treatment on the short-range order of the ionomers. In the pristine state, the lsc-PEM exhibited uniformly shorter T_1 compared to the ssc-PEM, which can be correlated with lower crystallinity[70] and higher water uptake[71] of the lsc-PEM.

For the lsc-PEM, T_1 across all groups decreased by ~20% (~30% for the SCF_2/CCF_2 signal) to 24 hours but recovered at longer treatment times. This trend indicated that there is an evolution of crystallinity in the lsc-PEM, with a decrease in order observed at the beginning of conditioning. Additionally, while T_1 of SCF_2/CCF_2 differed significantly for the pristine lsc-PEM, it aligned with the other functional groups after 72 h of Fenton treatment. It indicates a modification of spin diffusion behavior, which describes the equilibration of magnetic polarization along a polymer chain. For the pristine state, the regimes of the backbone and the polar sulfonic acid moieties were weakly coupled. With increasing Fenton treatment time, the coupling increased due to decreased separation between both regimes, resulting in equilibration of T_1. The evolution of the average T_1 of the ssc-PEM followed a similar trend to the lsc-PEM, but with a more pronounced initial decrease (~60%), indicating a greater loss of crystallinity. In contrast to the lsc-PEM, the SCF_2/CCF_2 T_1 fully equilibrated with the other functional groups regardless of Fenton treatment time, indicating a decreased separation between the regimes of the backbone and the short polar sulfonic acid moieties compared with the lsc-PEM.

Surface properties from contact angle and adhesion measurements

Building on molecular-level insights into mobility and crystallinity, contact angle (θ) measurements revealed distinct wettability trends during Fenton treatment (Fig. 9a and b).

The lsc-PEM displayed a progressive decrease in θ_{H_2O}, corresponding to increasing surface hydrophilicity, with a total reduction of ~20% over the treatment period. In contrast, the ssc-PEM demonstrated no consistent trend. The smaller apparent changes in the ssc-PEM are likely influenced by

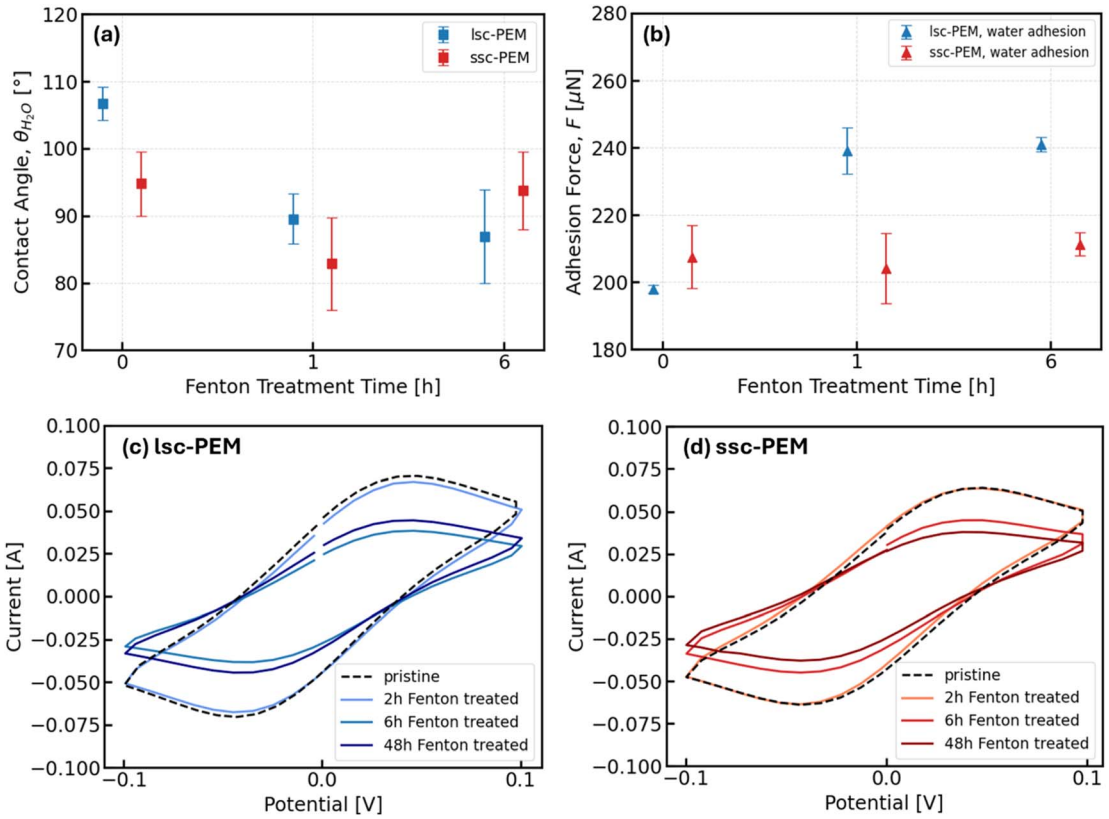

Fig. 9 | Effect of Fenton treatment on wettability, interfacial adhesion, and ionic permeability of lsc-PEM (blue) and ssc-PEM (red). (a) Water contact angles and (b) adhesion forces for water droplets measured on pristine membranes and after 1 and 6 h of treatment. Error bars represent standard deviations. (c and d) *I–V* curves of lsc-PEM and ssc-PEM in the pristine state and after 2, 6, and 48 h of Fenton treatment.

measurement variability, amplified by its higher inherent hydrophilicity and rapid swelling.

Adhesion force (F) measurements showed a pattern consistent with wettability. For lsc-PEM, water adhesion increased by ~21% after Fenton treatment, whereas ssc-PEM exhibited no statistically significant change.

Overall, Fenton treatment increased surface hydrophilicity and enhanced water adhesion strength in the lsc-PEM, while ssc-PEM remained largely unaffected. Results are summarized in Table S4 and S5.

Functional impact on ionic permeability from I–V measurements

I–V measurements (Fig. S9)[62,63] revealed comparable ionic permeability of pristine lsc-PEM and ssc-PEM membranes, while Fenton treatment reduced transmembrane ion current in both (Fig. 9c and d).

For lsc-PEM, current decreased moderately by ~5% at 100 mV after short exposure (2 h), followed by a pronounced ~46% drop at intermediate times (6 h) and partial recovery to ~37% below the pristine value after prolonged exposure (48 h). In contrast, ssc-PEM remained nearly stable initially, then declined gradually to ~30% at intermediate and ~41% at prolonged exposure.

Overall, Fenton treatment reduced ionic permeability in both membrane types. Lsc-PEM experienced an early, sharp loss with partial recovery, while ssc-PEM underwent a gradual, sustained decline.

These electrochemical trends, together with the structural, morphological, and interfacial changes observed earlier, form the basis for the following discussion on the multi-scale degradation behavior of PEMs under Fenton treatment. In particular, they support a mechanistic picture where intrinsic chemical structure changes are relatively minor, while oxygen accumulation drives morphological failure, reframing the interpretation of Fenton tests.

Discussion

Based on the portfolio of analytical techniques, the impact of accelerated Fenton degradation on PEMs can be grouped into chemical and morphological processes. The impact on PEM chemistry was assessed at the molecular scale by ^{19}F MAS-NMR, ATR-FTIR, and Raman spectroscopy, as well as IC. The impact on PEM morphology was examined at the nano- and mesoscale using SAXS, SEM, and ^{19}F T_1 relaxation, complemented by surface wettability and adhesion measurements. Finally, the functional impact of these chemical and structural changes was evaluated at the device level through *I–V* measurements.

Table 1 | Summary of PEM chemistry, morphology/structure, PEM surface and ion transport properties after *ex situ* Fenton accelerated stress testing

Category	Metric	Lsc-PEM	Ssc-PEM	Interpretation
Chemistry	F^- release (% of total F, IC)	7.14%	19.26%	Absolute chemical breakdown products released to liquid
	Spectroscopic fingerprint (NMR)	Slight drop in relative side chain signal (18% after 72 h)	No change in relative intensities signal	No clear selective peak loss; mainly uniform degradation
Morphology	Surface blister evolution (SEM)	Rapid growth; strong coalescence; distribution broadens to larger blisters	Slower growth; smaller, more uniform blisters; narrow distribution	Defects mainly due to O_2 evolution (side reaction under *ex situ* Fenton conditions)
Nano/meso structure	Ionomer peak (hydrophilic *d*-spacing) (SAXS)	q: 0.22 → 0.24 Å^{-1} (d: 28.6 → 26.2 Å)	Unchanged initially; disappears after long treatment	Hydrophilic domain change/ contraction; possibly linked to transport properties
	Matrix knee attenuation (SAXS)	Decreases during treatment; partial recovery later	Decreases; low-q upturn indicates aggregation	Reduced order in hydrophobic/crystalline regions
Surface properties	Adhesion force (F) and contact angle (θ)	Increased surface hydrophilicity and water adhesion	Largely unchanged	Changes likely morphological not chemical
Transport	Ion current change after 48 h (I–V)	−37% *vs.* pristine	−41% *vs.* pristine	Impact on through-plane ion transport

On the molecular scale, spectroscopy indicated only minor preferential degradation of polar side chain groups in case of lsc-PEM, as ^{19}F-NMR spectra indicated a slight decrease in the relative SCF_2/CCF_2 signal intensity, while at the same time a significant fluoride release was determined quantitatively by IC. In contrast, the ssc-PEM ^{19}F spectra exhibited no relative signal intensity changes, but still a significant fluoride loss was determined by IC as well. Therefore, by exclusion, chemical degradation during Fenton treatment must have occurred in a mainly sequential fashion, in which all chemical groups were eliminated uniformly. However, lsc- and ssc-PEM exhibited different degradation behaviors. First, bulk degradation, as indicated by NMR, and surface degradation, as indicated by optical spectroscopy, occurred at different rates for the two PEM materials. Second, overall chemical degradation emerged at significantly higher rates for the ssc-PEM. However, preferential degradation of the polar moieties was enhanced for the lsc-PEM in the bulk, while accelerated degradation of the sulfonic acid groups on the surface occurred mainly for the ssc-PEM. This behavior may result from different phase separations of hydrophilic and hydrophobic domains in the two ionomers. Here, as indicated by the spin diffusion behavior in the ^{19}F T_1 relaxation results, the pristine lsc-PEM exhibits a strong separation between the water-bearing percolation network and the polycrystalline PTFE-backbone phase. This, in turn, may lead to a hindrance of radical attack progression originating from the polar moiety. This separation and therefore steric hindrance is not as distinct in the ssc-PEM and therefore, degradation is more uniform and pronounced in the ssc-PEM. In addition, the slightly preferential radical attack on the polar end groups which was supposed from the ^{19}F signal ratios of the lsc-PEM could be associated with the contraction of hydrophilic domains which was derived from the shift of the ionomer peak in the SAXS spectra. A loss of SO_3H groups is associated with a decreasing stability of the hydrophilic channels.

While molecular scale degradation was limited, ionomer morphology was strongly affected. On the nano-to mesoscale, early Fenton treatment caused loss of crystallinity in both ionomers, seen by attenuation of the SAXS matrix knee and decreasing T_1.[61] With ongoing treatment, behaviors diverged. As the aforementioned features recover, the lsc-PEM recrystallizes, which is likely driven by the loss of amorphous hydrophilic segments. In addition, the formation of cross-linkings within the ionomer backbone from radical end groups formed by molecular degradation is also conceivable, although there is a lack of direct experimental evidence.[72] In contrast, the ssc-PEM experiences no recrystallization; however, a polymer aggregation occurs as implied by SAXS, suggesting partial reorganization of polymer chains.[69]

The accumulation of nano- and mesoscale alterations ultimately manifests as more pronounced mesoscale degradation. In the lsc-PEM, the surface developed a pitted topology that enhanced wetting, possibly shifting towards a Wenzel or partly impregnated regime.[73] Water penetration is further facilitated by features such as burst caps and slit-like tears. Overall, these morphological changes lower the apparent contact angle despite the intrinsic hydrophobicity of the lsc-PEM surface. Furthermore, the increase in water adhesion likely originates directly from the enhanced effective hydrophilic contact area due to the degraded topology. In contrast, ssc-PEM maintained constant contact angle and unchanged adhesion forces, consistent with less pronounced blistering.

Ultimately, the combined impact of chemical, morphological, and functional degradation governs ionic permeability. Both PEMs experienced an initial drop in transmembrane ion current, yet their long-term trends diverged. While the ssc-PEM exhibited a steady, monotonic decline, the lsc-PEM displayed

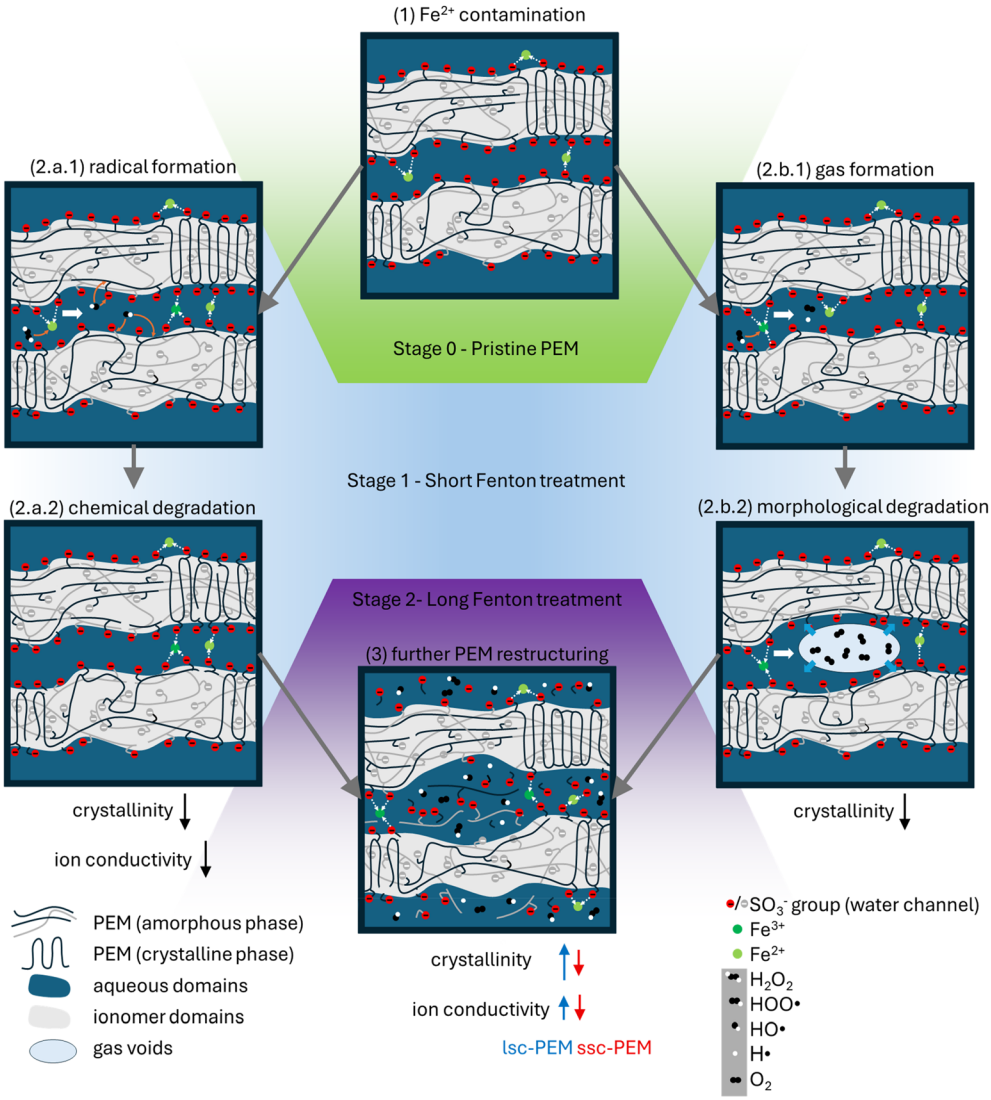

Fig. 10 Proposed mechanism of PFSA membrane degradation during an *ex situ* Fenton test employing the ion-exchange method. (1) Fe^{2+} cations are incorporated into the membrane by exchange with sulfonic acid protons. (2.a.1) Exposure to H_2O_2 generates radicals *via* the primary Fenton reactions. (2.a.2) Radical-induced reactions affect the polymer backbone and side chains. (2.b.1). Side reactions produce gaseous oxygen within the membrane. (2.b.2) Internal gas accumulation leads to void and blister formation. (3) Prolonged Fenton treatment increases both chemical and morphological changes, with distinct responses in the lsc-PEM and ssc-PEM.

partial current recovery after extended Fenton treatment. Permeability loss likely originated from increased ionic resistance due to nano- and mesoscale morphological changes, including amorphization and hydrophilic domain contraction, as only minor preferential breakdown of $-SO_3H$ charge carriers occurred. The partial recovery observed for lsc-PEM coincided with recrystallization of the ionomer, possibly restoring ion-conductive pathways.

Table 1 compiles the main observations for the lsc-PEM and ssc-PEM under identical conditions to facilitate comparison across the applied methods. It is intended to separate chemical indicators (*e.g.*, fluoride release) from morphology/transport indicators (*e.g.*, blisters/voids and *I–V* response) and to summarize trends.

Conclusion

The cross-scale observations from multi-technique analyses, ranging from chemical changes at the molecular scale (loss of functional groups and fluoride release), through morphological alterations at the nano- and mesoscales (loss of crystallinity, chain mobility, and surface restructuring), to functional consequences at the device level (reduced ionic permeability), reveal a degradation pathway linking structure and performance across multiple length scales, summarized in Fig. 10.

Fenton treatment employing the ion-exchange method begins with the replacement of sulfonic acid protons in the membrane by Fe^{2+} cations through soaking in an acidic $FeSO_4$ solution (Fig. 10(1)).[32] After exposure to H_2O_2, Fe^{2+} is oxidized to Fe^{3+}, producing highly reactive $HO^{\bullet}$ and $H^{\bullet}$ radicals

(Fig. 10(2.a.1); see also eqn (3) and (4)), which can initiate –SO_3H group cleavage, side chain scission, and backbone degradation (Fig. 10(2.a.2)). This leads to decreased ion-exchange capacity and crystallinity as revealed by *I–V*-measurements and SAXS. The occurrence of these radical-driven processes is supported by fluoride release measured *via* IC, which provides direct evidence of chemical breakdown.[38]

However, despite this chemical degradation, the observed surface blistering cannot be explained by chemical degradation alone. While H_2O_2 exposure alone has been reported to induce minor structural changes in PFSA membranes, the literature consistently shows that severe morphological damage, including internal void formation, occurs predominantly in simultaneous presence of transition metals, such as Fe^{2+}.[35,39] Therefore, in the present work, side reactions are hypothesized to dominate the physical alterations by generating O_2 (Fig. 10(2.b.1); eqn (10)–(12)):[17]

$$HOO^{\bullet} + H_2O_2 \rightarrow HO^{\bullet} + H_2O + O_2 \quad (10)$$

$$2HOO^{\bullet} \rightarrow H_2O_2 + O_2 \quad (11)$$

$$Fe^{3+} + HOO^{\bullet} \rightarrow Fe^{2+} + H^{+} + O_2 \quad (12)$$

Gas formation was evident as bubbling during Fenton treatment. O_2 then accumulates within the membrane, as low gas permeability inhibits rapid diffusion.

Because Fe^{2+} is introduced directly into the membrane, oxygen evolution occurs throughout the PEM. As pressure builds up internally, the membrane inflates, forming blisters that ultimately rupture (Fig. 10(2.b.2)), as confirmed by SEM. This inflation leads to the loss of the structural integrity of the membrane, as structured domains are displaced as indicated by SAXS.

For the lsc-PEM, recrystallization is hypothesized to occur once amorphous domains are degraded or removed, allowing the remaining backbone segments to align and pack efficiently. In addition, higher crystallinity could be promoted by the formation of new cross-linkings within the ionomer backbone from the interconnection of radical end groups. Moreover, if amorphous degradation fragments initially obstruct hydrophilic channels, their removal during extended treatment could clear these pathways, contributing to the observed partial recovery in ionic permeability. The aspects depicted in (Fig. 10(3)) are weighted differently for the ssc-PEM than for the lsc-PEM. A higher fluoride release provides evidence of enhanced membrane thinning. Additionally, the lack of recrystallization indicates a difference in the microstructure of hydrophilic and hydrophobic domains, as discussed in the literature.[74] These observations highlight the different degradation behaviors between long- and short-side-chain PEM materials during Fenton testing.

However, as *ex situ* Fenton tests induce additional morphological changes not evident in conventional PEM operations, conclusions regarding the effect of Fenton degradation on membrane properties, when based solely on *ex situ* Fenton tests, should be drawn with caution. The observed changes may not exclusively reflect the chemical degradation mechanisms relevant under actual PEMWE conditions due to the increased reagent concentration in the *ex situ* Fenton tests.

These multi-technique insights highlight the limitations of *ex situ* Fenton protocols in accurately representing degradation under operational conditions. The results pave the way for the development of applicable durability testing protocols and thus new synthesis strategies for stable ionomer membranes. To improve the relevance and effectiveness of these tests, the concentration of the Fenton reagent should be adjusted to ensure sufficient reaction rates while suppressing unwanted side reactions. Beyond reagent concentration, the experimental setup affects the type and interpretability of observed degradation features. Therefore, the value of *ex situ* testing can be increased by implementing *in operando* approaches. For example, a liquid SEM cell design could be utilized to monitor oxygen and blister formation. This design includes a continuous low-concentration supply of H_2O_2 and Fe^{2+}, which is also suggested in EU harmonized accelerated stress test protocols.[75]

Such adjustments would better mimic *in operando* degradation processes, enabling more accurate assessments of PEM durability. Beyond PEMs, these guidelines will support the development of standardized accelerated stress tests for ionomer-based materials in a broad range of electrochemical energy devices.

Author contributions

R. R. and J.-P. P. conceived the project, carried out the investigation, performed the formal analysis, prepared visualizations, and wrote the original draft. S. J. and J. P. contributed to the conceptualization and formal analysis, and to writing – review and editing. C. O., J. L., S. S., K. F., and D. T. D. carried out the investigation, performed the formal analysis, and contributed to writing – original draft. L. R. contributed to the investigation and formal analysis. A. W. performed the formal analysis and contributed to writing – review and editing. H. K. and S. B. contributed to writing – review and editing. E. J. and A. K. provided project administration and supervision and contributed to writing – review and editing. J. G. contributed to formal analysis and supervision, and to writing – review and editing. R.-A. E. contributed to conceptualization, funding acquisition, project administration, and supervision, and to writing – review and editing.

Conflicts of interest

The authors state that there are no conflicts of interest to declare.

Data availability

All data used in this manuscript is available for download at Jülich Data: https://doi.org/10.26165/JUELICH-DATA/GXOYTR.

Supplementary information (SI) is available. See DOI: https://doi.org/10.1039/d6ta01360k.

Acknowledgements

The authors gratefully acknowledge the financial support by the German Federal Ministry for Research, Technology and Aeronautics (BMFTR) through the H2Giga project DERIEL (grant number 03HY122C) and SEGIWA (grant number 03HY121B). Additionally, we would like to thank Dr Günter Schmid for his scientific contributions and for facilitating numerous discussions.

References

1 A. Bhaskar, R. Abhishek, M. Assadi and H. N. Somehesaraei, Decarbonizing primary steel production : Techno-economic assessment of a hydrogen based green steel production plant in Norway, *J. Clean. Prod.*, 2022, **350**, 131339, DOI: 10.1016/j.jclepro.2022.131339.

2 M. van der Spek, et al., Perspective on the hydrogen economy as a pathway to reach net-zero CO 2 emissions in Europe, *Energy Environ. Sci.*, 2022, **15**, 1034–1077, DOI: 10.1039/D1EE02118D.

3 P.-A. Le, et al., The current status of hydrogen energy: an overview, *RSC Adv.*, 2023, **13**, 28262–28287, DOI: 10.1039/D3RA05158G.

4 A. Javed, et al., Exploring the state-of-operation of proton exchange membrane electrolyzers, *Int. J. Hydrogen Energy*, 2025, **98**, 280–294, DOI: 10.1016/j.ijhydene.2024.12.055.

5 Y. Sun, et al., Advancements in cathode catalyst and cathode layer design for proton exchange membrane fuel cells, *Nat. Commun.*, 2021, **12**, 5984, DOI: 10.1038/s41467-021-25911-x.

6 K. Zhang, et al., Status and perspectives of key materials for PEM electrolyzer, *J. Nano Energy Power Res.*, 2022, **1**, e9120032, DOI: 10.26599/NRE.2022.9120032.

7 J. Borowec, et al., Proton Exchange Membrane Water Electrolyzer Cathode: A Nanomechanical and Nanoelectrical Analysis, *J. Electrochem. Soc.*, 2025, **172**, 54511, DOI: 10.1149/1945-7111/add213.

8 S. Siracusano, et al., Degradation issues of PEM electrolysis MEAs, *Renewable Energy*, 2018, **123**, 52–57, DOI: 10.1016/j.renene.2018.02.024.

9 I. Nicotera, L. Coppola and C. Simari, Enhancing sulfonated polyethersulfone performance by incorporating TiO2-decorated MWCNTs: A viable solution for high-temperature polymer electrolyte fuel cell applications, *Int. J. Hydrogen Energy*, 2024, **89**, 56–65, DOI: 10.1016/j.ijhydene.2024.09.282.

10 S. Finger, *et al.*, Degradation phenomena in PEMWE revealed by correlative electrochemical and nanostructure analysis, *Energy Environ. Sci.*, 2025, **18**(22), 9877, DOI: 10.1039/D5EE03712C.

11 S.-H. Shin, et al., Improving the Mechanical Durability of Short-Side-Chain Perfluorinated Polymer Electrolyte Membranes by Annealing and Physical Reinforcement, *ACS Omega*, 2019, **4**, 19153–19163, DOI: 10.1021/acsomega.9b02436.

12 Q. Feng, et al., A review of proton exchange membrane water electrolysis on degradation mechanisms and mitigation strategies, *J. Power Sources*, 2017, **366**, 33–55, DOI: 10.1016/j.jpowsour.2017.09.006.

13 N. Li, S. S. Araya and S. K. Kær, Long-term contamination effect of iron ions on cell performance degradation of proton exchange membrane water electrolyser, *J. Power Sources*, 2019, **434**, 226755, DOI: 10.1016/j.jpowsour.2019.226755.

14 H. Becker, et al., Impact of impurities on water electrolysis: a review, *Sustain. Energy Fuels*, 2023, **7**, 1565–1603, DOI: 10.1039/D2SE01517J.

15 N. Wolf, *et al.*, Tuning Proton Exchange Membrane Electrolytic Cell Performance by Conditioning Nafion N115-Based Membrane Electrode Assemblies, *Electrochem. Sci. Adv.*, 2025, **5**(3), e202400038, DOI: 10.1002/elsa.202400038.

16 C. Dong, et al., Self-cycled photo-Fenton-like system based on an artificial leaf with a solar-to-H2O2 conversion efficiency of 1.46, *Nat. Commun.*, 2022, **13**, 4982, DOI: 10.1038/s41467-022-32410-0.

17 M. Zatoń, J. Rozière and D. J. Jones, Current understanding of chemical degradation mechanisms of perfluorosulfonic acid membranes and their mitigation strategies: a review, *Sustain. Energy Fuels*, 2017, **1**, 409–438, DOI: 10.1039/C7SE00038C.

18 D. Yu, et al., Electronic structure modulation of iron sites with fluorine coordination enables ultra-effective H2O2 activation, *Nat. Commun.*, 2024, **15**, 2241, DOI: 10.1038/s41467-024-46653-6.

19 A. Bosnjakovic and S. Schlick, Nafion Perfluorinated Membranes Treated in Fenton Media: Radical Species Detected by ESR Spectroscopy, *J. Phys. Chem. B*, 2004, **108**, 4332–4337, DOI: 10.1021/jp037519c.

20 P. Trinke, B. Bensmann and R. Hanke-Rauschenbach, Experimental evidence of increasing oxygen crossover with increasing current density during PEM water electrolysis, *Electrochem. Commun.*, 2017, **82**, 98–102, DOI: 10.1016/j.elecom.2017.07.018.

21 M. Schalenbach, M. Carmo, D. L. Fritz, J. Mergel and D. Stolten, Pressurized PEM water electrolysis: Efficiency and gas crossover, *Int. J. Hydrogen Energy*, 2013, **38**, 14921–14933, DOI: 10.1016/j.ijhydene.2013.09.013.

22 E. Endoh, S. Terazono, H. Widjaja and Y. Takimoto, Degradation Study of MEA for PEMFCs under Low Humidity Conditions, *Electrochem. Solid-State Lett.*, 2004, **7**, A209, DOI: 10.1149/1.1739314.

23 Z. Rui, et al., A new insight into the chemical degradation of proton exchange membranes in water electrolyzers, *J. Mater. Chem. A*, 2024, **12**, 9563–9573, DOI: 10.1039/D3TA05224A.

24 E. Kuhnert, et al., Impact of intermittent operation on photovoltaic-PEM electrolyzer systems: A degradation study based on accelerated stress testing, *Int. J. Hydrogen Energy*, 2024, **55**, 683–695, DOI: 10.1016/j.ijhydene.2023.11.249.

25 S. H. Frensch, et al., Impact of iron and hydrogen peroxide on membrane degradation for polymer electrolyte membrane water electrolysis: Computational and experimental investigation on fluoride emission, *J. Power*

Sources, 2019, **420**, 54–62, DOI: 10.1016/j.jpowsour.2019.02.076.

26 L. Ghassemzadeh, K.-D. Kreuer, J. Maier and K. Müller, Chemical Degradation of Nafion Membranes under Mimic Fuel Cell Conditions as Investigated by Solid-State NMR Spectroscopy, *J. Phys. Chem. C*, 2010, **114**, 14635–14645, DOI: 10.1021/jp102533v.

27 L. Gubler, S. M. Dockheer and W. H. Koppenol, Radical (HO • , H • and HOO •) Formation and Ionomer Degradation in Polymer Electrolyte Fuel Cells, *J. Electrochem. Soc.*, 2011, **158**, B755–B769, DOI: 10.1149/1.3581040.

28 A. Bosnjakovic, M. K. Kadirov and S. Schlick, Using ESR spectroscopy to study radical intermediates in proton-exchange membranes exposed to oxygen radicals, *Res. Chem. Intermed.*, 2007, **33**, 677–687, DOI: 10.1163/156856707782169372.

29 K. H. Wong and E. Kjeang, Macroscopic In-Situ Modeling of Chemical Membrane Degradation in Polymer Electrolyte Fuel Cells, *J. Electrochem. Soc.*, 2014, **161**, F823–F832, DOI: 10.1149/2.0031409jes.

30 Z. Rui and J. Liu, Understanding of free radical scavengers used in highly durable proton exchange membranes, *Prog. Nat. Sci. Mater. Int.*, 2020, **30**(6), 732–742, DOI: 10.1016/j.pnsc.2020.08.013.

31 L. Ghassemzadeh, K. D. Kreuer, J. Maier and K. Müller, Evaluating chemical degradation of proton conducting perfluorosulfonic acid ionomers in a Fenton test by solid-state 19F NMR spectroscopy, *J. Power Sources*, 2011, **196**, 2490–2497, DOI: 10.1016/j.jpowsour.2010.11.053.

32 S. Kundu, L. C. Simon and M. W. Fowler, Comparison of two accelerated Nafion™ degradation experiments, *Polym. Degrad. Stab.*, 2008, **93**, 214–224, DOI: 10.1016/j.polymdegradstab.2007.10.001.

33 F. C. Teixeira, A. P. Teixeira and C. M. Rangel, Chemical stability of new nafion membranes doped with bisphosphonic acids under Fenton oxidative conditions, *Int. J. Hydrogen Energy*, 2023, **48**, 37489–37499, DOI: 10.1016/j.ijhydene.2023.04.063.

34 A. Fernicola, M. A. Navarra and S. Panero, Aprotic ionic liquids as electrolyte components in protonic membranes, *J. Appl. Electrochem.*, 2008, **38**, 993–996, DOI: 10.1007/s10800-008-9514-6.

35 T. Kinumoto, et al., Durability of perfluorinated ionomer membrane against hydrogen peroxide, *J. Power Sources*, 2006, **158**, 1222–1228, DOI: 10.1016/j.jpowsour.2005.10.043.

36 L. Fiedler, *et al.*, Stability of Bipolar Plate Materials for Proton-Exchange Membrane Water Electrolyzers: Dissolution of Titanium and Stainless Steel in DI Water and Highly Diluted Acid, *ChemElectroChem*, 2023, **10**(20), e202300373, DOI: 10.1002/celc.202300373.

37 L. Ghassemzadeh and S. Holdcroft, Quantifying the structural changes of perfluorosulfonated acid ionomer upon reaction with hydroxyl radicals, *J. Am. Chem. Soc.*, 2013, **135**, 8181–8184, DOI: 10.1021/ja4037466.

38 H. Tang, S. Peikang, S. P. Jiang, F. Wang and M. Pan, A degradation study of Nafion proton exchange membrane of PEM fuel cells, *J. Power Sources*, 2007, **170**, 85–92, DOI: 10.1016/j.jpowsour.2007.03.061.

39 K. Hongsirikarn, X. Mo, J. G. Goodwin and S. Creager, Effect of H2O2 on Nafion® properties and conductivity at fuel cell conditions, *J. Power Sources*, 2011, **196**, 3060–3072, DOI: 10.1016/j.jpowsour.2010.11.133.

40 F. C. Teixeira, A. P. Teixeira and C. M. Rangel, Chemical stability of new nafion membranes doped with bisphosphonic acids under Fenton oxidative conditions, *Int. J. Hydrogen Energy*, 2023, **48**, 37489–37499, DOI: 10.1016/j.ijhydene.2023.04.063.

41 A. C. Fernandes and E. A. Ticianelli, A performance and degradation study of Nafion 212 membrane for proton exchange membrane fuel cells, *J. Power Sources*, 2009, **193**, 547–554, DOI: 10.1016/j.jpowsour.2009.04.038.

42 M. Robert, A. El Kaddouri, J.-C. Perrin, J. Raya and O. Lottin, Time-resolved monitoring of composite Nafion™ XL membrane degradation induced by Fenton's reaction, *J. Membr. Sci.*, 2021, **621**, 118977, DOI: 10.1016/j.memsci.2020.118977.

43 H. J. Lim, G. Kim and G. J. Yun, Durability and Performance Analysis of Polymer Electrolyte Membranes for Hydrogen Fuel Cells by a Coupled Chemo-mechanical Constitutive Model and Experimental Validation, *ACS Appl. Mater. Interfaces*, 2023, **15**, 24257–24270, DOI: 10.1021/acsami.2c15451.

44 W. Shi and L. A. Baker, Imaging heterogeneity and transport of degraded Nafion membranes, *RSC Adv.*, 2015, **5**, 99284–99290, DOI: 10.1039/C5RA20291D.

45 S. Thiel and M. Eichelbaum, Scanning electrochemical microscopy for the differentiation of radical-induced degradation mechanisms in polymer electrolyte membranes, *RSC Adv.*, 2024, **14**, 13748–13757, DOI: 10.1039/D4RA02203C.

46 L. Gubler and W. H. Koppenol, Kinetic Simulation of the Chemical Stabilization Mechanism in Fuel Cell Membranes Using Cerium and Manganese Redox Couples, *J. Electrochem. Soc.*, 2011, **159**, B211–B218, DOI: 10.1149/2.075202jes.

47 F. Fouda-Onana, et al., Investigation on the degradation of MEAs for PEM water electrolysers part I: Effects of testing conditions on MEA performances and membrane properties, *Int. J. Hydrogen Energy*, 2016, **41**, 16627–16636, DOI: 10.1016/j.ijhydene.2016.07.125.

48 E. Kuhnert, M. Heidinger, D. Sandu, V. Hacker and M. Bodner, Analysis of PEM Water Electrolyzer Failure Due to Induced Hydrogen Crossover in Catalyst-Coated PFSA Membranes, *Membranes*, 2023, **13**, 348, DOI: 10.3390/membranes13030348.

49 M. Mukaddam, Y. Wang and I. Pinnau, Structural, Thermal, and Gas-Transport Properties of Fe3+ Ion-Exchanged Nafion Membranes, *ACS Omega*, 2018, **3**, 7474–7482, DOI: 10.1021/acsomega.8b00914.

50 K. Kunimatsu, B. Bae, K. Miyatake, H. Uchida and M. Watanabe, ATR-FTIR study of water in Nafion membrane combined with proton conductivity

measurements during hydration/dehydration cycle, *J. Phys. Chem. B*, 2011, **115**, 4315–4321, DOI: 10.1021/jp112300c.
51 P. H. C. Eilers & H. F. M. Boelens, *Baseline Correction With Asymmetric Least Squares Smoothing*, Leiden University Medical Centre Report, 2005, 1, 5.
52 M. Newville, T. Stensitzki, D. B. Allen & A. Ingargiola, *LMFIT: Non-linear Least-Square Minimization and Curve-Fitting for Python*, Zenodo, 2014.
53 D. A. Skoog, F. J. Holler & S. R. Crouch, *Principles of Instrumental Analysis*, Cengage Learning, Australia, 2018.
54 M. Danilczuk, L. Lin, S. Schlick, S. J. Hamrock and M. S. Schaberg, Understanding the fingerprint region in the infra-red spectra of perfluorinated ionomer membranes and corresponding model compounds: Experiments and theoretical calculations, *J. Power Sources*, 2011, **196**, 8216–8224, DOI: 10.1016/j.jpowsour.2011.05.067.
55 C. R. Harris, et al., Array programming with NumPy, *Nature*, 2020, **585**, 357–362, DOI: 10.1038/s41586-020-2649-2.
56 The pandas development team, *Pandas-Dev/Pandas: Pandas*, Zenodo, 2025.
57 The Matplotlib Development Team. *Matplotlib: Visualization with Python*, Zenodo, 2025.
58 M. Waskom, seaborn: statistical data visualization, *JOSS*, 2021, **6**, 3021, DOI: 10.21105/joss.03021.
59 C. A. Schneider, W. S. Rasband and K. W. Eliceiri, NIH Image to ImageJ: 25 years of image analysis, *Nat. Methods*, 2012, **9**, 671–675, DOI: 10.1038/nmeth.2089.
60 R. Gommers et al, *Scipy/Scipy: SciPy 1.16.0*, Zenodo, 2025.
61 S.-Y. Choi, M. M. Ikhsan, K. S. Jin and D. Henkensmeier, Nanostructure-property relationship of two perfluorinated sulfonic acid (PFSA) membranes, *Intl J of Energy Research*, 2022, **46**, 11265–11277, DOI: 10.1002/er.7926.
62 K. Froehlich, et al., Fabrication of soft-etched nanoporous polyimide membranes for ionic conduction and discrimination, *J. Membr. Sci.*, 2021, **617**, 118633, DOI: 10.1016/j.memsci.2020.118633.
63 K. Froehlich, M. C. Scheuerlein, M. Ali, S. Nasir and W. Ensinger, Enhancement of heavy ion track-etching in polyimide membranes with organic solvents, *Nanotechnology*, 2021, **33**, 45301, DOI: 10.1088/1361-6528/ac2f5a.
64 Q. Chen and K. Schmidt-Rohr, 19 F and 13 C NMR Signal Assignment and Analysis in a Perfluorinated Ionomer (Nafion) by Two-Dimensional Solid-State NMR, *Macromolecules*, 2004, **37**, 5995–6003, DOI: 10.1021/ma049759b.
65 L. Helm, Relaxivity in paramagnetic systems: Theory and mechanisms, *Prog. Nucl. Magn. Reson. Spectrosc.*, 2006, **49**, 45–64, DOI: 10.1016/j.pnmrs.2006.03.003.
66 R. P. S. Chakradhar, G. Sivaramaiah, J. L. Rao and N. O. Gopal, Fe(3+) ions in alkali lead tetraborate glasses–an electron paramagnetic resonance and optical study, *Spectrochim. Acta, Part A*, 2005, **62**, 51–57, DOI: 10.1016/j.saa.2004.12.004.
67 C. H. Taboy, K. G. Vaughan, T. A. Mietzner, P. Aisen and A. L. Crumbliss, Fe3+ coordination and redox properties of a bacterial transferrin, *J. Biol. Chem.*, 2001, **276**, 2719–2724, DOI: 10.1074/jbc.m004763200.
68 A. Kusoglu and A. Z. Weber, New Insights into Perfluorinated Sulfonic-Acid Ionomers, *Chem. Rev.*, 2017, **117**, 987–1104, DOI: 10.1021/acs.chemrev.6b00159.
69 P. C. van der Heijden, L. Rubatat and O. Diat, Orientation of Drawn Nafion at Molecular and Mesoscopic Scales, *Macromolecules*, 2004, **37**, 5327–5336, DOI: 10.1021/ma035642w.
70 S. Mbarek, N. El Kissi, Z. Baccouch and C. Iojoiu, Extrusion of Nafion and Aquivion membranes: environmentally friendly procedure and good conductivities, *Polym. Bull.*, 2019, **76**, 1151–1166, DOI: 10.1007/s00289-018-2427-6.
71 T. Flottat, B. Latour, F. Goujon, P. Hauret and P. Malfreyt, Investigating percolation and clustering effects on aquivion and nafion membranes at the molecular scale, *Int. J. Hydrogen Energy*, 2023, **48**, 33283–33296, DOI: 10.1016/j.ijhydene.2023.05.086.
72 M. Nishida, T. Tanaka, Y. Hayakawa and M. Nishida, Solid-State Nuclear Magnetic Resonance (NMR) and Nuclear Magnetic Relaxation Time Analyses of Molecular Mobility and Compatibility of Plasticized Polyhydroxyalkanoates (PHA) Copolymers, *Polymers*, 2018, **10**, 506, DOI: 10.3390/polym10050506.
73 E. E. Ubuo, I. A. Udoetok, A. T. Tyowua, I. O. Ekwere and H. S. Al-Shehri, The Direct Cause of Amplified Wettability: Roughness or Surface Chemistry?, *J. Compos. Sci.*, 2021, **5**, 213, DOI: 10.3390/jcs5080213.
74 C. Wang, et al., Evaluation of the microstructure of dry and hydrated perfluorosulfonic acid ionomers: microscopy and simulations, *J. Mater. Chem. A*, 2013, **1**, 938–944, DOI: 10.1039/C2TA01034H.
75 K. T. Malkow, EU harmonised accelerated stress testing protocols for low-temperature water electrolyser. A proposal with testing guidance for assessing performance degradation in water electrolyser stacks, *Europäische Kommission*, 2024, DOI: 10.2760/988717.

